JGR Solid Earth

RESEARCH ARTICLE
10.1029/2019JB018922

Spatiotemporal Properties of Sub-Rayleigh and Supershear Ruptures Inferred From Full-Field Dynamic Imaging of Laboratory Experiments

V. Rubino[1], A. J. Rosakis[1], and N. Lapusta[2,3]

[1]Graduate Aerospace Laboratories, California Institute of Technology, Pasadena, CA, USA, [2]Mechanical and Civil Engineering, California Institute of Technology, Pasadena, CA, USA, [3]Seismological Laboratory, California Institute of Technology, Pasadena, CA, USA

Key Points:
- We produce evolving maps of displacements and particle velocities for sub-Rayleigh/supershear laboratory ruptures
- The maps confirm the structure of the near-tip fields previously available only from theoretical and numerical models
- The measurements enable us to quantify the attenuation characteristics of the off-fault motion

Supporting Information:
- Supporting Information S1
- Movie S1
- Movie S2
- Movie S3
- Movie S4

Correspondence to:
V. Rubino,
vito.rubino@caltech.edu

Citation:
Rubino, V., Rosakis, A. J., & Lapusta, N. (2020). Spatiotemporal properties of sub-Rayleigh and supershear ruptures inferred from full-field dynamic imaging of laboratory experiments. *Journal of Geophysical Research: Solid Earth*, *125*, e2019JB018922. https://doi.org/10.1029/2019JB018922

Received 21 OCT 2019
Accepted 11 JAN 2020
Accepted article online 15 JAN 2020

Abstract Many earthquakes propagate at sub-Rayleigh speeds. Earthquakes propagating at supershear speeds, though less common, are by far more destructive. Hence, it is important to quantify the motion characteristics associated with both types of earthquake ruptures. Here we report on the spatiotemporal properties of dynamic ruptures measured in our laboratory experiments using the dynamic digital image correlation technique. Earthquakes are mimicked by the frictional rupture propagating along the interface of two Homalite plates. Digital images of the propagating ruptures are captured by an ultrahigh-speed camera and processed with digital image correlation in order to produce sequences of evolving displacement and velocity maps. Our measurements reveal the full-field structure of the velocity components, bridge the gap between previous spatially sparse velocimeter measurements available only at two to three locations, and enable us to quantify the attenuation patterns away from the interface.

1. Introduction

Most earthquakes propagate at subshear rupture speeds V_r, that is, at speeds less than the shear wave speed c_s (Das, 2007). Supershear rupture propagation speeds, higher than the shear wave speed but lower than the pressure wave speed c_p, had been surmised by theoretical predictions and numerical simulations (Andrews, 1976; Burridge, 1973) and have been observed for most large strike-slip events. Some examples of earthquakes inferred to propagate at supershear speed include 1906 San Francisco earthquake (Song et al., 2008), 1979 Imperial Valley earthquake (Archuleta, 1984; Spudich & Cranswick, 1984), 1992 Landers earthquake (Olsen et al., 1997), 1999 Izmit earthquake (Bouchon et al., 2001), 2001 Kunlun earthquake (Bouchon & Vallée, 2003), 2002 Denali earthquake (Ellsworth et al., 2004), and more recently the 2018 magnitude 7.5 Palu earthquake (Bao et al., 2019; Socquet et al., 2019). While supershear ruptures are less common than sub-Rayleigh ones, it is important to study them as supershear propagation can cause much larger shaking far from the fault than sub-Rayleigh ruptures (Andrews, 2010; Bernard & Baumont, 2005; Bhat et al., 2007; Dunham & Archuleta, 2005; Dunham & Bhat, 2008). Theoretical predictions and numerical simulations are based on assumptions about the fault kinematics or the fault rheology that affect a wide range of earthquake mechanics issues. For example, assumptions about the evolution of friction can result in a dramatically different behavior in terms of energy partitioning, rupture speed, residual stress levels on faults, patterns of seismic and aseismic slip, and ground motion (Ben-Zion, 2001; Brune et al., 1969; Heaton, 1990; Jiang & Lapusta, 2016; Kanamori & Rivera, 2006; Lu et al., 2007; Noda et al., 2009; Noda & Lapusta, 2013; Shi et al., 2008; Zheng & Rice, 1998). This points toward the need of well-instrumented laboratory measurements.

Dynamic rupture propagation, including sub-Rayleigh and supershear ruptures, has been observed in numerous experimental studies (e.g., Bayart et al., 2016; Ben-David et al., 2010; Mello et al., 2010; Mello et al., 2016; Nielsen et al., 2010; Passelègue et al., 2013; Rosakis et al., 1999; Rosakis et al., 2007; Rosenau et al., 2017; Rubinstein et al., 2004; Schubnel et al., 2011; Svetlizky et al., 2017; Svetlizky & Fineberg, 2014; Xia et al., 2004). However, most experiments employed either temporally accurate but spatially sparse diagnostics, such as velocimeters and strain gages, or semiquantitative full-field measurements (e.g., photoelasticity) with low temporal resolution. Acoustic emissions were used in a large body of work on laboratory earthquake analogs to determine source properties as well as other rupture features (e.g., Goebel et al., 2012; Lei & Ma, 2014; McLaskey & Lockner, 2016; Passelègue et al., 2016), while other techniques were able to

measure the contact area as it evolved with rupture propagation (e.g., Rubinstein et al., 2004; Selvadurai & Glaser, 2015) but these approaches could not measure full-field quantities, such as velocities or strains. Recently, some experimental setups have been developed to image the full-field rupture behavior, employing either acoustic imaging, based on ultrasound (Latour et al., 2011), or digital image correlation (DIC; Caniven et al., 2015). Employing acoustic imaging has enabled to simultaneously image, in real time, two planes, parallel and perpendicular to the sliding interface, respectively, but it has to use hydrogels as model materials in order to significantly reduce the shear wave speed and thus the speed of the propagating rupture (Latour et al., 2011). Some experiments with the DIC method (Caniven et al., 2015) lack adequate temporal resolution to fully capture rapidly propagating ruptures.

Here we present the first full-field dynamic characterization of sub-Rayleigh and supershear ruptures by using the DIC method coupled with ultrahigh-speed photography (Rubino et al., 2015; Rubino et al., 2019). In our laboratory setup, dynamic rupture propagates along a frictional interface in an analog material (typically Homalite-100 or PMMA). Earlier versions of this setup have been used to demonstrate a number of key rupture dynamics phenomena, including supershear transition, bimaterial effect, off-fault attenuation and damage, pulse-like to crack-like transition, and rupture interaction with the free surface (Gabuchian et al., 2017; Lu et al., 2007; Lu et al., 2010; Mello et al., 2010, 2014; Ngo et al., 2012; Xia et al., 2004; Xia et al., 2005). In these studies, measurements captured the time history of selected velocity components at two to three locations per test, and they were not able to provide a unifying picture of the spatial variations of the velocity components. Recently, we have enhanced the diagnostics of our laboratory setup by including ultrahigh-speed photography with a single camera vision system in combination with DIC, in order to map temporal evolution of a wealth of field quantities, including displacements, velocities, strains, strain rates, and stresses (Rubino et al., 2019). This development has allowed us to study phenomena that were undetectable before, such as the evolution of dynamic friction (Rubino et al., 2017) and the formation of pressure shock fronts (Gori et al., 2018). Here, we show that our full-field measurements, while consistent with previous point-wise velocimeter measurements and numerical simulations, can explain the pattern of deformation across the entire field of view of observation and can be used to quantify the spatiotemporal properties of dynamic ruptures.

2. Laboratory Setup to Quantify the Full-Field Behavior of Dynamic Ruptures

2.1. Laboratory Earthquake Setup

Earthquakes are simulated in the laboratory by dynamic ruptures propagating along the frictional interface of two quadrilateral plates made of a polymer, Homalite-100 in this study, inclined of an angle α (Figure 1). The specimen assembly is loaded in compression by a uniaxial load P, so that the interface is prestressed in compression and shear with $\sigma_0 = P\cos^2\alpha$ and $\tau_0 = P\sin\alpha\cos\alpha$, respectively. The frictional interface is first polished, in order to erase any machining defects, and then bead blasted with microbeads with the sizes of 104–211 μm, in order to introduce a controlled roughness (Lu et al., 2010; Mello et al., 2010; Rubino et al., 2019). Ruptures are nucleated by the disintegration of a NiCr wire placed across the interface and connected to a capacitor bank with a set voltage.

An important characteristic of the ruptures produced in our laboratory setup is that, once nucleated, they propagate spontaneously, driven by the far-field stresses σ_0 and τ_0. The rupture speed (ranging from sub-Rayleigh to supershear) and rupture mode (crack like vs. pulse like) depend on the combination of P and α (Lu et al., 2010). The investigation of this parameter space indicates that larger loads and steeper inclination angles result in supershear cracks, while lower loads and shallower angles produce sub-Rayleigh pulses with intermediate behaviors, including supershear pulses and sub-Rayleigh cracks (Lu et al., 2010). In particular, sub-Rayleigh ruptures can be produced at comparatively higher loads when using shallower angles. One such configuration that will be discussed in the following is $P = 12$ MPa and $\alpha = 24°$, which produces sub-Rayleigh pulses. Since ruptures produced with larger levels of prestress have a better signal-to-noise ratio, we select this experimental configuration to study sub-Rayleigh ruptures. On the other hand, to study supershear ruptures, we select a steeper inclination angle, $\alpha = 29°$, and a level of prestress depending on the rupture speed regime to be obtained. We choose $P = 4.5$ and 23–25 MPa, for a slower and faster rupture, respectively. Dynamic ruptures produced in our laboratory setup are highly repeatable as documented in previous studies (e.g., Lu et al., 2010; Rosakis et al., 2007). The ruptures presented in this study, selected

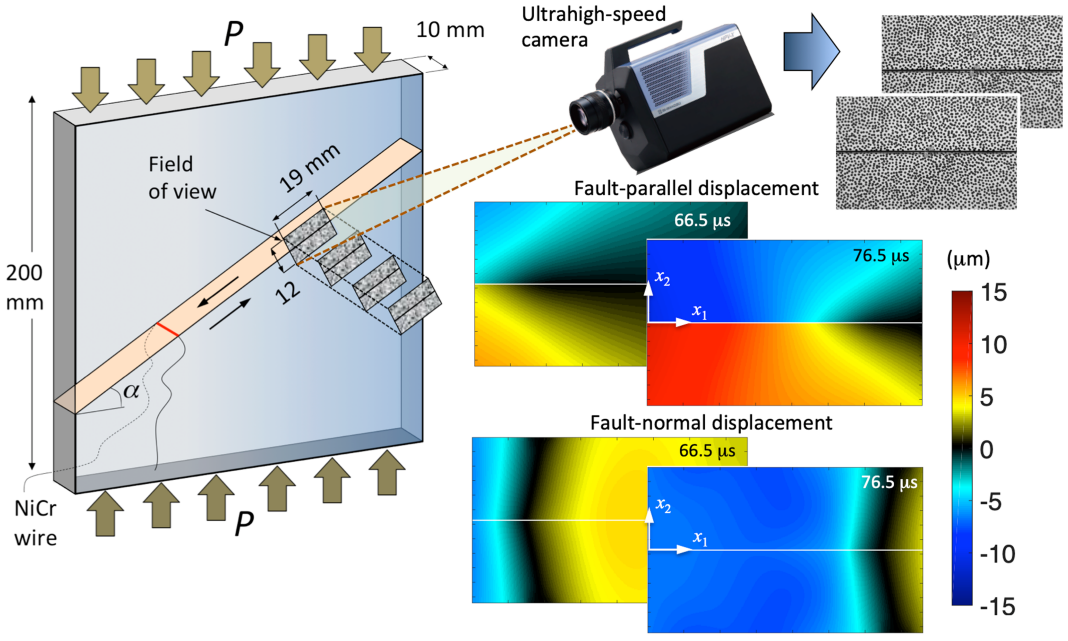

Figure 1. Schematics of the laboratory earthquake setup used to produce sub-Rayleigh and supershear rupture and to quantify their full-field behavior using ultrahigh-speed photography and digital image correlation (DIC). Dynamic ruptures propagate along the oblique interface, inclined of an angle α, of two quadrilateral plates of Homalite, simulating a fault in the Earth's crust. The specimen is loaded axially with a uniform compressive pressure P. Ruptures are nucleated by the pressure released by the electrical discharge of a NiCr wire placed across the specimen's interface. The applied load P and interface inclination angle α control the rupture speed and mode. An ultrahigh-speed camera captures a sequence of textured images (at 1–2 million frames/sec), which are analyzed with the digital image correlation method and are used to infer the displacement and velocity fields. The full-field maps depict the fault-parallel and fault-normal displacements of a sub-Rayleigh rupture obtained with $P = 12$ MPa and $\alpha = 24°$.

from a large set of experiments, provide characteristic behavior for each of the experimental conditions explored.

2.2. Ultrahigh-Speed DIC Diagnostics Employed to Quantify Dynamic Ruptures

We employ the ultrahigh-speed photography, based on a single camera vision system, in combination with 2D-DIC (Sutton et al., 2009) in order to quantify the full-field behavior of dynamic ruptures (Rubino et al., 2019). The diagnostics comprise an ultrahigh-speed camera (Shimadzu HPV-X), a white light source (Cordin 605), a high-voltage capacitor (Cordin 640), and a pulse generator (575 Series, Berkeley Nucleonics Corp.) to introduce controlled delay between individual elements of the diagnostics, and an oscilloscope (Tektronix® DPO-3034) to monitor the signals. The ultrahigh-speed camera is equipped with a fixed focal distance telephoto lens (see Rubino et al. (2019) for details) and is rotated about the camera's optic axis by an angle α, so as to align its pixels with the specimen's interface and facilitate the DIC analysis. Digital images of a portion of the specimen are acquired at 1–2 million frames per second, depending on the rupture speed, with an exposure time of 200 ns and at a resolution of 400×250 pixels^2.

The size of the imaged area of the specimen, or field of view (FOV), ranges within a broad span, from 19×12 up to 131×82 mm^2, depending on whether the aim is to image rupture features in the far field or to achieve a high level of accuracy (Rubino et al., 2019). In this study, we focus on ruptures imaged with a small field of view (19×12 mm^2) in order to accurately capture the behavior in the near field. We also report the case of a rupture imaged with a large field of view (131×82 mm^2) to study the far-field rupture features. Image and image analysis parameters are reported in Table S1 of the supporting information, according to the International Digital Image Correlation Society guidelines (Jones & Iadicola, 2018). The area of the specimen to be imaged is coated by a white paint and subsequently textured by a black speckle pattern in order to provide a characteristic gray-level signature to the images. The sequence of deformed digital images is then processed by a 2D-DIC software (Vic-2D by Correlated Solutions Inc.), which performs image

matching in order to provide the full-field maps of the displacement components $u_1(x_1, x_2, t)$ and $u_2(x_1, x_2, t)$ (Figure 1). The digital correlations are performed over image subsets (typically 41×41 pixels^2 in our analysis) that are overlapped with a step of 1 pixel. Displacement maps of u_1 and u_2 are then postprocessed using a nonlocal filter (Ayoub et al., 2009; Buades et al., 2006, 2008; Rubino et al., 2015; Rubino et al., 2019).

The image correlation is performed over two independent domains, above and below the interface, in order to preserve the fault-parallel displacement discontinuities. Standard local DIC techniques can compute the displacement fields only up to half a subset away from the boundary, which is an important limitation if one wants to capture the rupture behavior very close to the fault. In order to overcome this limitation, the DIC software we employ (Vic-2D by Correlated Solutions Inc.) has been specifically modified to extrapolate displacements all the way to the interface, using affine transformation functions (Rubino et al., 2019). Since the correlation is performed independently over the two domains and there is no continuity constraint imposed, the measurement noise can result in displacement fields containing small deviation from symmetry or antisymmetry. We address this issue by using the "symmetry-adjustment" procedure described in Rubino et al. (2019), based on the symmetric and antisymmetric properties of the fault-normal and fault-parallel displacement fields, respectively.

The velocity fields $\dot{u}_1(x_1, x_2, t)$ and $\dot{u}_2(x_1, x_2, t)$ are computed from the sequence of the displacement components $u_1(x_1, x_2, t)$ and $u_2(x_1, x_2, t)$, using a central difference scheme. The velocity magnitude fields are then computed as $|\dot{\mathbf{u}}| = \sqrt{\dot{u}_1^2 + \dot{u}_2^2}$. Strains are also obtained via the central difference scheme, and stresses are computed using linear elastic constitutive properties with a Poisson's ratio of $\nu = 0.35$ and dynamic Young's modulus of $E = 5.3$ GPa, corresponding to the high strain rate properties of Homalite-100 (Rubino et al., 2019; Singh & Parameswaran, 2003).

2.3. Assessing Triggering Delays and determining the Time After Rupture Initiation

In order to determine the time after rupture initiation and correctly plot time histories and compare them with wave arrival times, we need to pinpoint the time when the rupture actually starts propagating. To do that, we need to assess the various delays involved in the triggering procedure. The Cordin 605 light source takes about 100 μs to ramp up to its maximum intensity and maintains it for approximately 1 ms. In order to guarantee a uniform level of lighting during the image acquisition process, the Cordin 605 source is triggered 200 μs ahead of the high-voltage capacitor used to initiate dynamic rupture, via the delay generator. This arrangement guarantees that, by the time images are acquired by the high-speed camera, the light intensity has already reached a stable plateau level with minimal oscillations. The high-speed camera has a delay t_{camera} with respect to the capacitor signal, which is set depending on the size and position of the field of view, as well as on the expected rupture speed.

Selected experiments were conducted imaging the rupture nucleation region. Careful analysis of these tests, in particular of the image sequence of the NiCr wire detonation, reveals that the wire burst starts 8 μs after the trigger signal to the high-voltage capacitor. Simultaneously, the displacement and velocity maps obtained via DIC from the same image sequence indicate that the rupture initiation occurs at the same time as the wire burst begins, with a delay of $t_{\text{ini}} = 8$ μs to the trigger from the capacitor bank. Another time delay is associated with the high-speed camera recording procedure. The high-speed camera continuously records images to a buffer memory at the set frame rate and exposure time. When it receives a trigger signal, it transfers the images from the buffer to permanent memory storage. The first image of the recorded sequence is the closest to the triggering signal and has a time delay t_{rec} to the trigger that is less than the interframe time.

In the analysis of time histories in this work, we use the time from rupture initiation defined by $t = t_{\text{a}} + t_{\text{camera}} + t_{\text{rec}} - t_{\text{ini}}$, where t_{a} is the acquisition time obtained from the high-speed camera at the set frame rate and starting with the camera triggering, t_{camera} is the camera delay to trigger, t_{rec} is the recording time delay, and t_{ini} is the rupture initiation delay with respect to the capacitor trigger. In previous studies employing ultrahigh-speed DIC, we have reported the time after triggering the test, $t = t_a + t_{\text{camera}}$ (Gori et al., 2018; Rubino et al., 2017, 2019). In this study, since we interpret the velocity time histories and wave arrival times, it is important to account for the rupture initiation delay, as well as all other delays mentioned above.

2.4. Rupture Speed Computation From the Experimental Measurements

The rupture speed V_r is computed by tracking the rupture tip along the interface. The rupture tip position as a function of time is obtained from the rupture arrival times at each location along the interface, which are determined by the time the slip rate function exceeds a set threshold V_{thr}, in analogy with numerical simulations (Liu & Lapusta, 2008; Needleman, 1999). The threshold is chosen to be just above the noise level, and therefore, it depends on the signal-to-noise ratio and sampling rate, which vary for different rupture modes and speeds. In the presented calculations, we choose V_{thr} in the range of 0.5–2 m/s. The slip rate is obtained at every pixel along the interface from the fault-parallel velocity maps (Figure 2), as the difference of the particle velocities immediately above and below the interface. Since the time at which the slip rate exceeds the threshold may not coincide with an actual data point, a linear interpolation is performed between frames right before and after exceeding V_{thr}. The rupture speed is then computed from the rupture tip position function describing its location along the interface as a function of time, by a central difference scheme. A Butterworth filter is used to smooth both the rupture tip position as a function of time before differentiation and the rupture speed versus position.

3. Full-Field Properties of Sub-Rayleigh and Supershear Ruptures

The model material employed in our experiments, Homalite-100, has a strain rate-dependent behavior (Singh & Parameswaran, 2003), resulting in a heterogeneous effective material properties field (Gori et al., 2018; Rubino et al., 2019). Since it is the local wave speeds that control the rupture speed, we will refer to these hereafter when indicating the rupture speed regime. For example, when we refer to supershear ruptures, we mean $V_r > c_s^{HSR}$, where c_s^{HSR} is the local high strain rate shear wave speed. Note that for Homalite-100, $c_s^{HSR} = 1.28$ and $c_p^{HSR} = 2.6$ km/s are the high strain rate shear and pressure wave speeds (Mello et al., 2010), respectively, and the high strain rate Rayleigh wave speed is $c_R^{HSR} = 0.92\, c_s^{HSR} = 1.18$ km/s. These wave speeds have been measured by tracking the pressure and shear wave fronts in sequences of photoelastic images (Mello et al., 2010; 2016). The low strain rate properties can be estimated using the Young's modulus ($E^{LSR} = 2.17$ GPa) measured at low strain rate ($\dot{\varepsilon} = 10^{-5}\ s^{-1}$) by Singh and Parameswaran (2003) and assuming effective linear elastic relations. The low strain rate shear wave speed yields $c_s^{LSR} = \sqrt{\mu^{LSR}/\rho} = 0.82$ km/s, where $\mu^{LSR} = E^{LSR}/2(1+\nu) = 0.804$ GPa is the low strain rate shear modulus and $\rho = 1{,}200$ kg/m^3 and $\nu = 0.35$ are the density and Poisson's ratio of Homalite, which are taken as strain rate invariants. Assuming a linear elastic relation between the shear and pressure wave speeds and a state of plane stress yields $c_p^{LSR} = \sqrt{2/1-\nu}\, c_s^{LSR} = 1.44$ km/s. Note that the high strain rate wave speeds are also consistent with the wave speeds computed following a similar procedure, assuming linear elastic relations and using the effective elastic properties of the material at high strain rate given by Singh and Parameswaran (2003).

3.1. Comparison Between a Sub-Rayleigh and a Supershear Rupture With $V_r > \sqrt{2} c_s^{HSR}$

Let us start by analyzing two ruptures whose speed is sub-Rayleigh and supershear, respectively.

A selection of snapshots describing the temporal evolution of the velocity components of the sub-Rayleigh and supershear ruptures is shown in Figure 2 (see also supporting information Movies S1 and S2). The two ruptures propagate at $V_r = 1.14$ and $V_r = 2.28$ km/s, respectively, where the rupture speeds are computed using the procedure detailed in section 2.4. Note that the fields are cropped, and their size is slightly smaller than that of the acquired speckled images. The sub-Rayleigh rupture is obtained with an applied vertical load of $P = 12$ MPa and an inclination angle of $\alpha = 24°$, which results in a normal and shear prestress levels of $\sigma_0 = P\cos^2\alpha = 10$ MPa and $\tau_0 = P\sin\alpha\cos\alpha = 4.5$ MPa, respectively. The loading configuration for the supershear rupture is $P = 23$ MPa and an inclination angle of $\alpha = 29°$, which results in a normal and shear prestress levels of $\sigma_0 = P\cos^2\alpha = 17.6$ MPa and $\tau_0 = P\sin\alpha\cos\alpha = 9.8$ MPa, respectively. These experimental conditions are known from past experiments to produce sub-Rayleigh and supershear ruptures, respectively (Lu et al., 2010). The left-lateral ruptures enter the field of view from the left and propagate in the positive x_1 direction. The fault-parallel velocities of both dynamic ruptures indicate a marked shear motion (Figures 2a and 2c). The fault-normal velocities are distinctively different between the two cases, with the sub-Rayleigh rupture being characterized by large regions of initially positive and subsequently negative velocity, forming

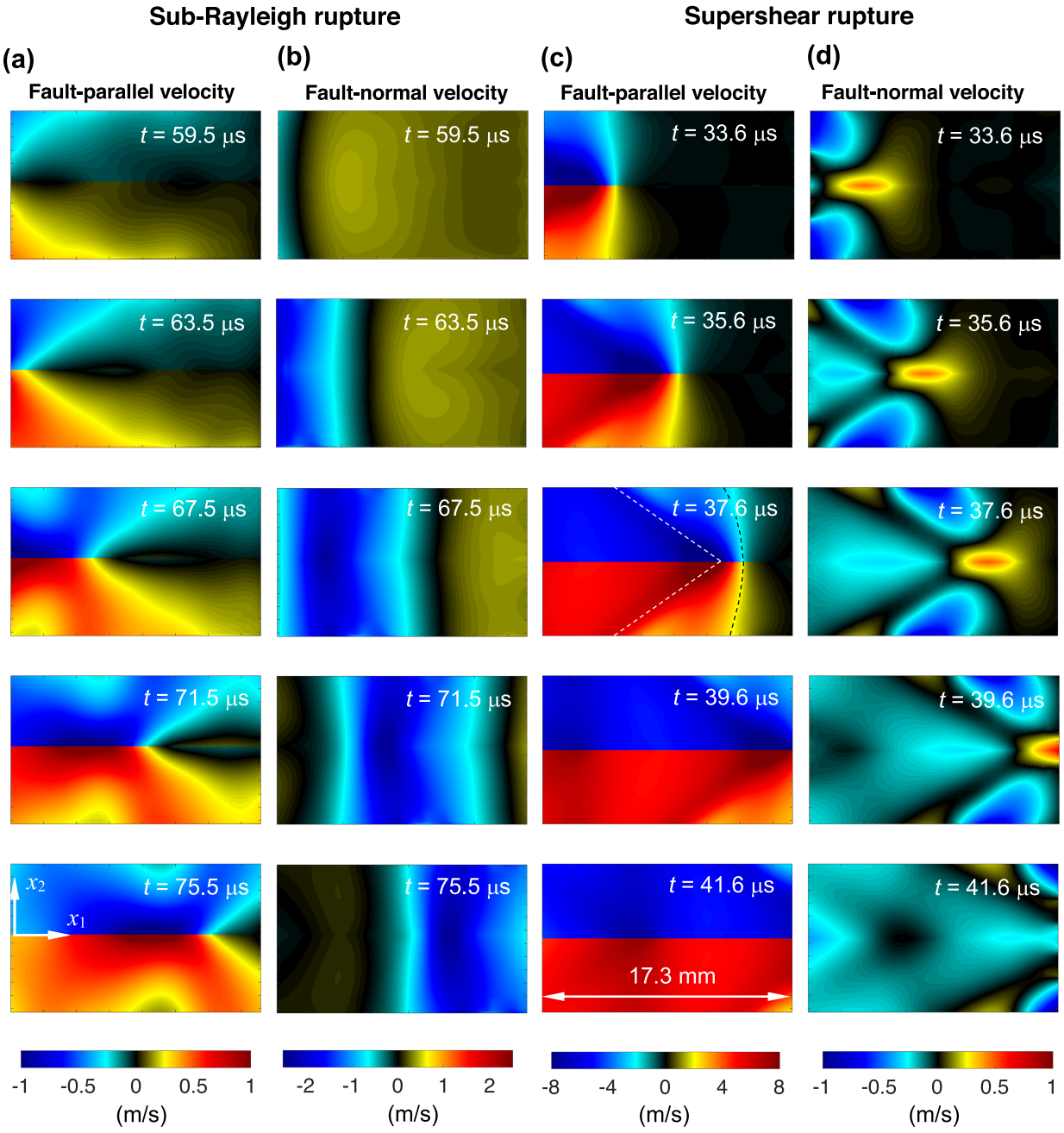

Figure 2. Full-field velocity snapshots for a sub-Rayleigh and supershear rupture. (a) Fault-parallel and (b) fault-normal velocities of the sub-Rayleigh rupture (with $V_r < c_R^{HSR}$) obtained with $P = 12$ MPa and $\alpha = 24°$. (c) Fault-normal and (d) fault-parallel velocities of a supershear rupture (with $V_r > \sqrt{2}c_s^{HSR}$) obtained with $P = 23$ MPa and $\alpha = 29°$. The supershear rupture is reproduced from Rubino et al. (2017) and Rubino et al. (2019). Note that the velocity field of the sub-Rayleigh rupture is governed by fault-normal motion, while that of the supershear rupture is governed by fault-parallel motion. The white and black dashed lines represent the shear and pressure shock fronts, respectively.

an elongated, peanut-like shape perpendicular to the fault, while the fault-normal velocity of the supershear rupture changes in sign moving from the fault to the far field.

One prominent feature displayed by all supershear ruptures is the presence of the shear Mach fronts radiating from the rupture tip; another prominent feature of supershear ruptures in viscoelastic materials is the pressure shock fronts formed by the dilatational field, ahead of the shear shock front (Gori et al., 2018; Rubino et al., 2019). While these features are best imaged using large fields of view where the shock fronts are fully developed, we also observe them in the near-tip field (white and black dashed lines in

Figure 2c). The formation of pressure shock fronts should not be possible in isotropic linear elastic solids (Freund, 1998; Needleman, 1999; Rosakis, 2002; Rosakis et al., 2007). In a recent study, we have shown that pressure shock fronts can indeed develop during propagation of dynamic ruptures in viscoelastic solids (Gori et al., 2018). As ruptures propagate, they induce a heterogeneous strain rate field, with larger strain rates in the near-rupture tip field compared to the far field. Due to the high strain rate sensitivity of Homalite-100 used in these tests, the wave speeds are increased in the near-tip field, where the strain rates are high (Gori et al., 2018; Rubino et al., 2019). Dynamic shear ruptures can then become supersonic with respect to the far-field pressure wave speed, as a result of the material viscoelastic behavior (Gori et al., 2018), while still staying below the local pressure wave speed in accordance with linear elastic theories (Freund, 1998; Needleman, 1999; Rosakis, 2002; Rosakis et al., 2007). Indeed, this is the case for the rupture of Figures 2c and 2d.

The rupture speed analysis indicates that the rupture of Figures 2a and 2b indeed propagates at a sub-Rayleigh rupture speed ($V_r = 1.14 < c_R^{\mathrm{HSR}} = 1.18$ km/s) throughout the entire imaging window considered in this experiment, while the rupture of Figures 2c and 2d propagates at supershear speed (with $V_r = 2.28 > c_s^{\mathrm{HSR}} = 1.28$ km/s), as shown by plotting the rupture speed V_{r} versus position along the interface, within the field of view imaged in our experiment (Figures 3a and 3b for the sub-Rayleigh and supershear, respectively). Note that the supershear rupture is also supersonic with respect to the far-field low strain rate pressure speed estimated above, as $V_r = 2.28 > c_p^{\mathrm{LSR}} = 1.44$ km/s. The supershear rupture of Figures 2c and 2d also propagates at a speed different from the Eshelby speed $\sqrt{2}\, c_s^{\mathrm{HSR}} = 1.81$ km/s, which has important implications on the radiated field. One of them is the formation of distinct shock fronts, as seen above. Another supershear rupture that propagates at $V_r \sim \sqrt{2}\, c_s^{\mathrm{HSR}}$, and for which the shock features tend to disappear, is discussed in section 3.2.

To emphasize the full-field velocity patterns of the dynamic ruptures shown in Figure 2, snapshots of the fault-parallel and fault-normal components are presented with overlaid contour plots in Figures 4 and 5, respectively. The snapshots are given at a time t = 69.5 and t = 37.6 μs after rupture initiation, for the sub-Rayleigh and supershear rupture, respectively. The fault-parallel velocity map of the sub-Rayleigh rupture is characterized by two lobes, associated with the dilatational field, propagating ahead of the rupture tip (Figures 2a and 4a). Behind the rupture tip, the velocity discontinuity across the interface clearly shows the propagating shear rupture, with the peak slip rate $\dot{\delta}(x_1, t) = \dot{u}_1(x_1 = 0^-, x_2, t) - \dot{u}_1(x_1 = 0^+, x_2, t)$ of ~2.4 m/s. The fault-parallel velocity of the supershear rupture shows a more pronounced shear motion (Figures 2b and 4b), with the peak slip rate in excess of 20 m/s. As noted above, the velocity field of the supershear rupture is characterized by shear Mach fronts as well as by the presence of pressure Mach fronts, forming because $V_r = 2.28$ km/s $> c_p^{\mathrm{LSR}}$. In contrast, the dilatational field lobes associated with the sub-Rayleigh rupture tend to extend ahead of the rupture tip due to the rupture speed being less then 50% of the local pressure wave speed (Figure 4a).

As both ruptures shown here propagate in the positive x_1 direction, unzipping the fault with a fault-parallel displacement and velocity discontinuity, they also display a motion in the direction perpendicular to the fault (Figures 2b and 2d). The continuity of the fault-normal displacement and velocity fields across the fault indicates that the fault moves in the direction perpendicular to its plane without opening. The sub-Rayleigh rupture presents a positive peanut-like-shaped region of vertical motion (in the positive x_2 direction) covering the entire height of the field of view, just ahead of the rupture tip (Figures 2a and 2b), indicating that the fault starts moving in the fault-normal direction before rupture arrival. As the sub-Rayleigh rupture swipes through the interface, the fault moves in the opposite (negative x_2) direction with a similar peanut-shaped pattern. Note that, while the fault-parallel velocity tapers gradually after attaining a peak, the fault-normal velocity goes to zero right behind the rupture tip (as discussed further below). The fault-normal velocity field of the supershear rupture displays a small region of positive motion around the interface, emanating from the rupture tip (Figures 2d and 5b). Two lobes of negative velocity extend from the rupture tip, outside of the region of positive motion, and are bounded by the dilatational and shear shock fronts (Rubino et al., 2019). These two negative lobes are followed by two narrow wedges hosting small positive motion and a large wedge of negative fault-normal velocity, starting just behind the rupture tip.

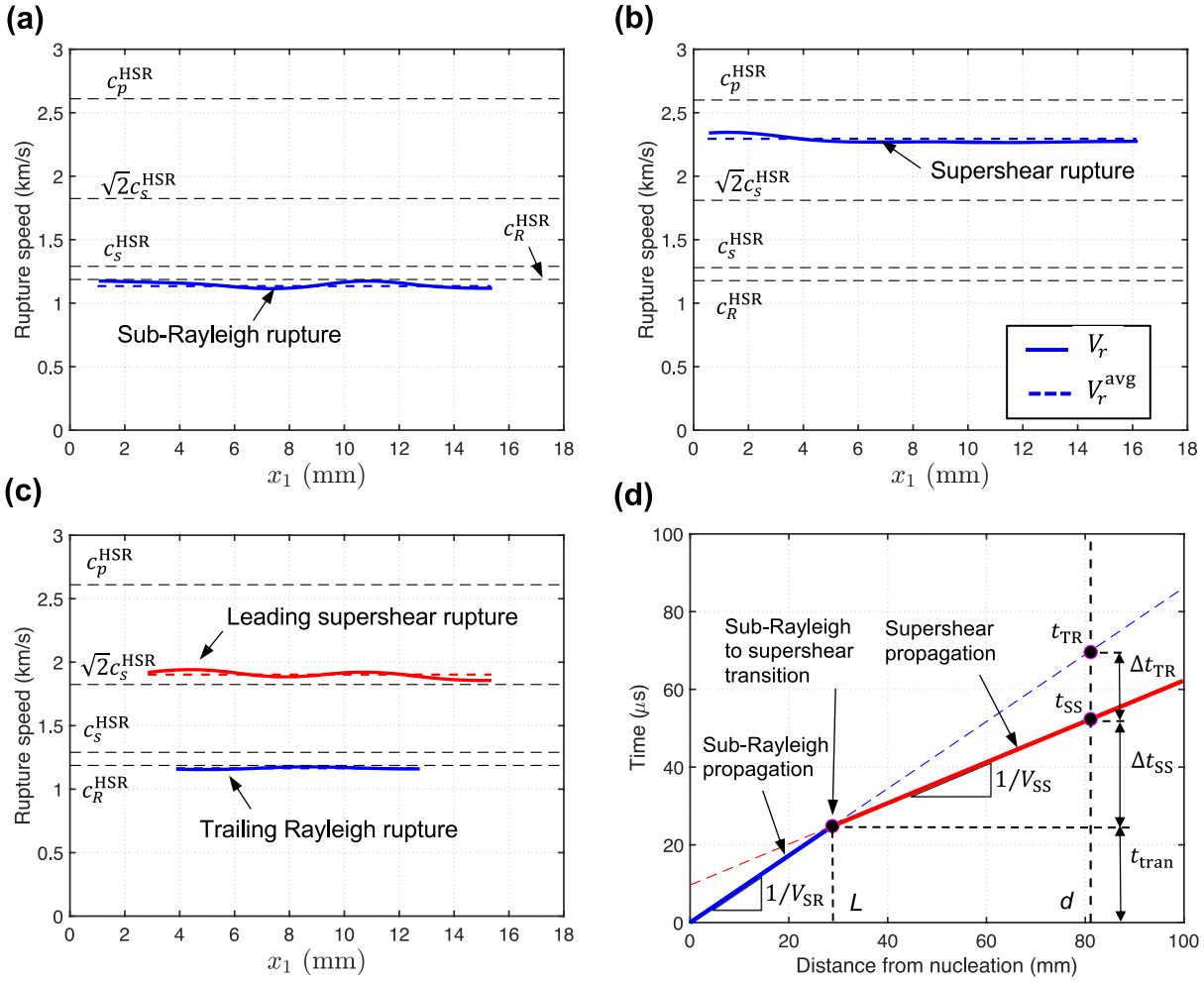

Figure 3. Experimentally obtained rupture speed versus position along the interface. Rupture speed tracked for three rupture cases discussed in this paper: (a) sub-Rayleigh, (b) supershear, propagating at $V_r > \sqrt{2}c_s^{HSR}$, and (c) supershear propagating at $V_r \sim \sqrt{2}c_s^{HSR}$. The rupture propagating at $V_r \sim \sqrt{2}c_s^{HSR}$ also features a distinct trailing Rayleigh rupture. (d) Supershear transition distance L, estimated using the rupture speeds measured in Figure 3c and the measured arrival times of Figure 10a. The rupture speed is computed from the rupture arrival times at pixels along the interface, determined using the slip rate time series.

In order to better understand the structure of the velocity field, the fault-parallel and fault-normal velocity components are plotted along paths parallel and perpendicular to the interface in Figures 4c–4f and 5c–5f, respectively, for the sub-Rayleigh (left) and supershear (right) ruptures. These plots are produced using the same snapshots of the velocity fields, at times t = 69.5 and t = 37.5 μs after rupture initiation, for the sub-Rayleigh and supershear ruptures, respectively, as these snapshots fully reveal the transient behavior at the rupture tip. Curves are plotted every three pixels, corresponding to every 134–140 μm, depending on the exact size of field of view (the two experiments have slightly different pixel sizes). Plotting the fault-parallel velocity along paths parallel to the interface shows that curves traced right on the fault are characterized by one prominent peak, while curves traced away from the fault display a double peak, for both the sub-Rayleigh (Figure 4c) and supershear (Figure 4d) ruptures. The first peak is associated to the dilatational field and the second to the shear field. On the fault, the two peaks coincide. Tracking the fault-parallel velocity on paths perpendicular to the fault and sweeping a region from ahead to behind the rupture tip reveals the marked velocity discontinuity across the interface in both cases of sub-Rayleigh and supershear rupture, Figures 4e and 4f, respectively.

For the sub-Rayleigh rupture, the fault-normal velocity plotted along the fault exhibits a negative peak at x_1~5.6 mm (Figure 5c), just behind the rupture tip. The rupture tip is identified at x_1~8 mm, assuming a threshold of 0.5 m/s in the slip rate. Note that since the fault-parallel velocity is antisymmetric, this slip

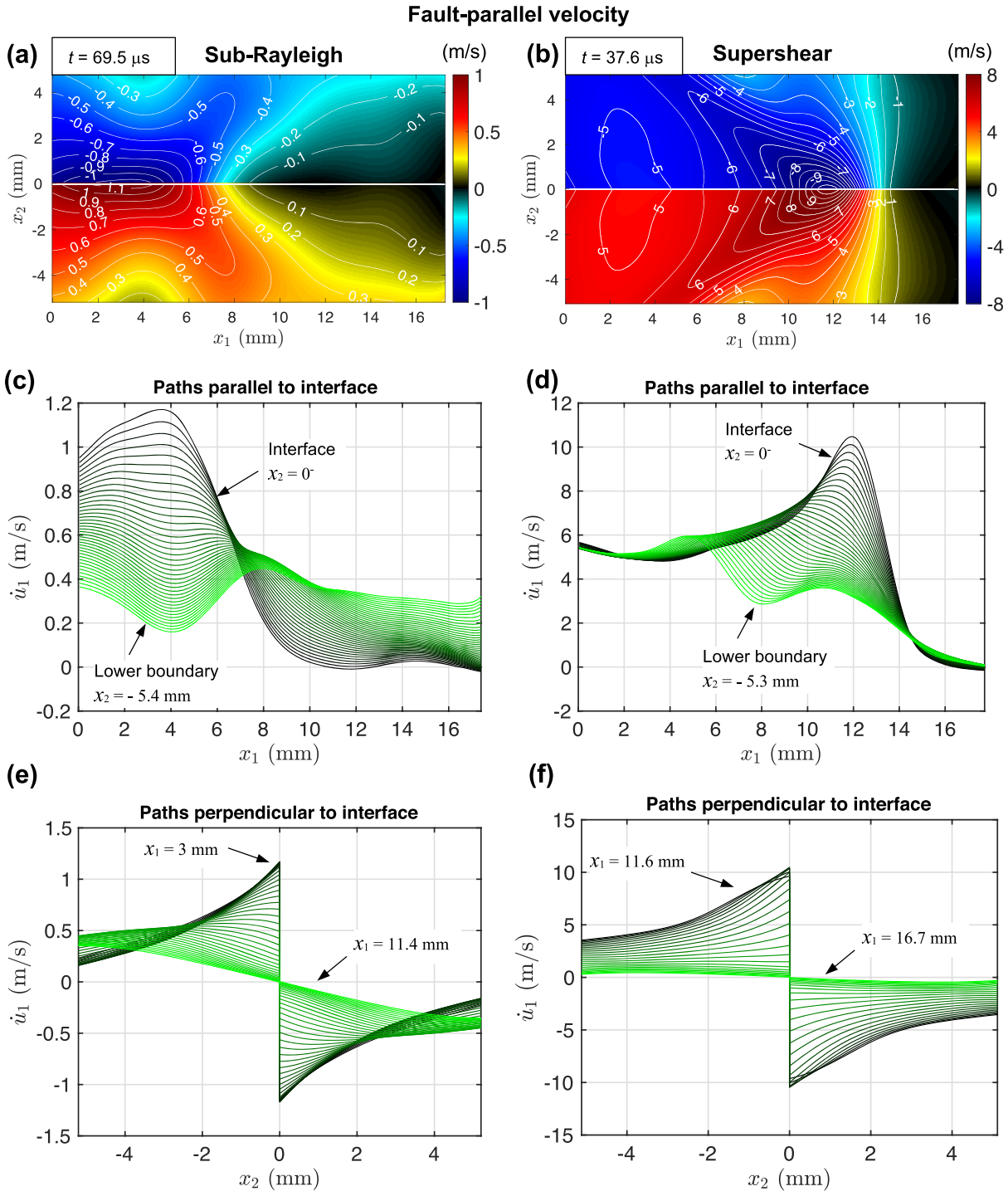

Figure 4. Fault-parallel velocity maps for the sub-Rayleigh (left) and supershear (right) ruptures, at times t = 69.5 and t = 37.6 μs after nucleation, respectively. (a, b) Contour plots overlapped on full-field maps. (c, d) Particle velocity along paths parallel to the interface (x_2 = const). Curves are plotted every 3 pixels (~0.14 mm). (e–f) Particle velocity along paths perpendicular to the interface (x_1 = const). Curves are plotted every 5 pixels (~0.23 mm).

rate threshold translates to a threshold of 0.25 m/s in Figure 4c. As the region of fault-normal velocity has a peanut-like shape bent forward, the peak in $\dot{u}_2$ tends to move slightly forward with distance from the fault (e.g., the peak is at x_1~6 mm at a distance from the fault of x_2~ − 4 mm) and only mildly attenuates (Figure 5e). For the supershear rupture, the fault-normal velocity plotted along the interface displays a positive peak followed by a negative peak, with a gradual transition to an inverted polarity at distance of

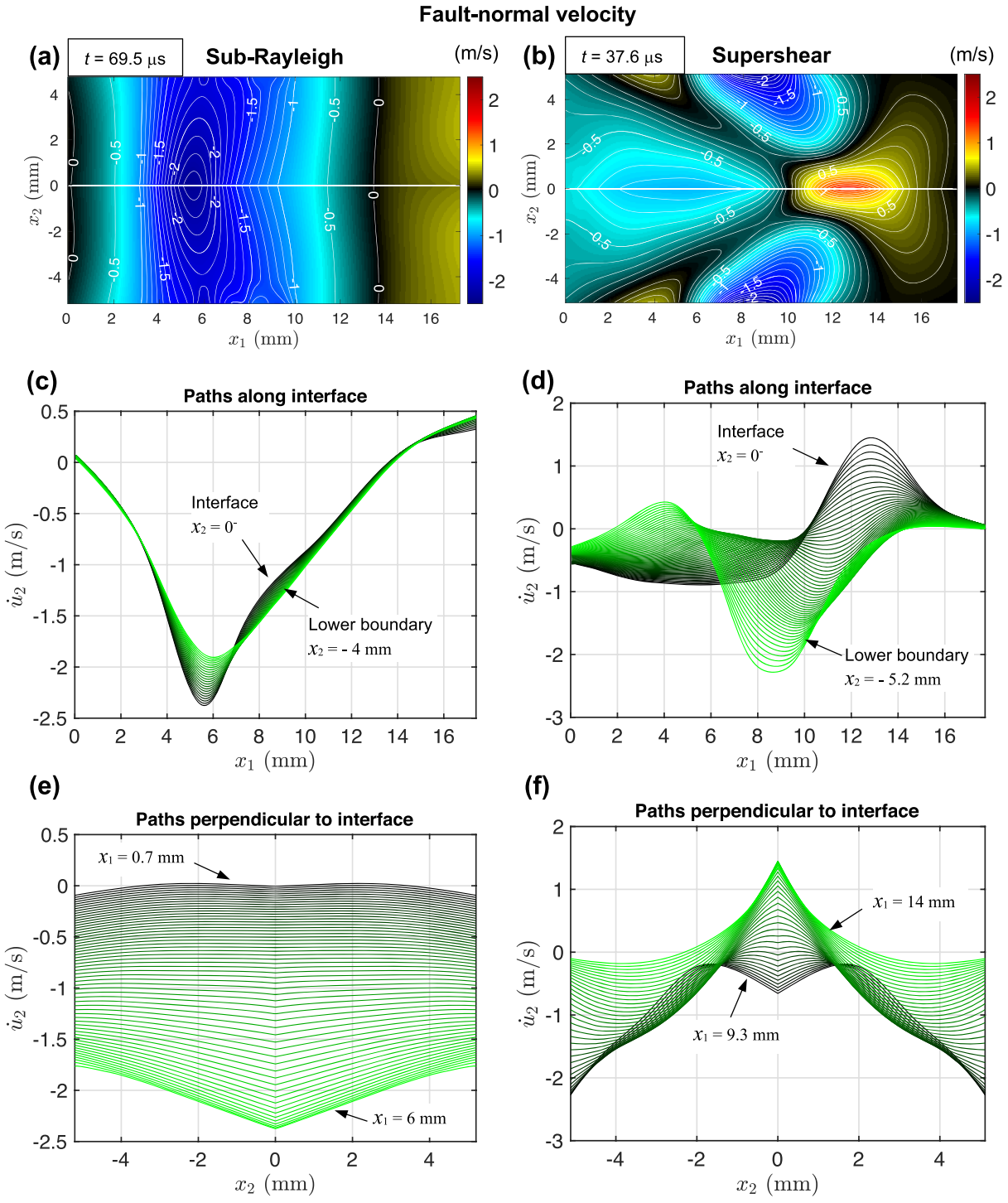

Figure 5. Fault-normal velocity maps for the supershear (left) and sub-Rayleigh (right) ruptures, at times $t = 69.5$ and $t = 37.6$ μs after nucleation, respectively. (a, b) Contour plots overlapped on full-field maps. (c, d) Particle velocity along paths parallel to the interface (x_2 = const.). Curves are plotted every 4 and 2 pixels for the supershear and sub-Rayleigh ruptures, respectively (corresponding to 0.18 and 0.09 mm, respectively). (e, f) Particle velocity along paths perpendicular to the interface (x_1 = const.). Curves are plotted every 2 pixels (0.09 mm) and 3 pixels (0.14 mm), respectively.

~5 mm from the fault (Figure 5d). Plotting the fault-normal velocity along paths perpendicular to the interface reveals the presence of the region of positive $\dot{u}_2$, concentrated around the interface, followed by two wedges of negative $\dot{u}_2$ radiating from the rupture tip in the far field (Figures 5b and 5f).

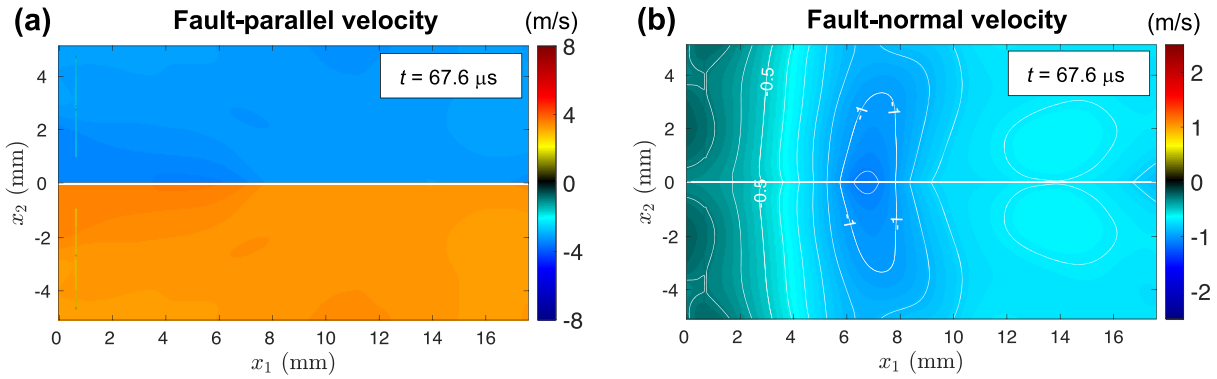

Figure 6. Full-field maps of the (a) fault-parallel and (b) fault-normal particle velocities of the same supershear rupture of Figures 4 and 5, at $t = 67.6$ μs after nucleation. At this time, the supershear rupture tip has already traversed the entire field. The fault-normal velocity field indicates the arrival of a Rayleigh wave, and its pattern resembles that of a sub-Rayleigh rupture (Figure 5b); the arrival time at the observation window is also consistent with a wave traveling at c_R^{HSR}. The fault-parallel velocity field at this time frame is nearly uniform and indicates a very mild secondary slip disturbance (see also Figure 9b at $t = 67.6$ μs). The arrival of a Rayleigh wave without an associated strong trailing slip, together with the supershear rupture arrival time consistent with a nearly constant rupture propagation, indicates that this rupture nucleated and propagated as supershear straight away and did not transition to supershear speed following the Burridge-Andrews mechanism or that it transitioned to supershear straight after nucleation with a very small transition distance.

One question regarding the supershear rupture is how it transitions from sub-Rayleigh to supershear speed. One typical transition mechanism is the Burridge-Andrews mechanism, according to which a shear stress peak (initially below shear strength) traveling in front of the main sub-Rayleigh rupture at the shear wave speed reaches the shear strength and gives rise to a secondary crack which then propagates at supershear speeds (Andrews, 1976; Burridge, 1973; Rosakis et al., 2007; Xia et al., 2004). Typically, when the supershear transition occurs according to this mechanism, the secondary supershear crack leaves behind the initial sub-Rayleigh crack that originated it, as a trailing Rayleigh slip disturbance. This characteristic Rayleigh signature has been observed before in a number of previous studies (e.g., Mello et al., 2010; Xia et al., 2004). If the supershear rupture presented in Figures 2–5 transitioned according to the Burridge-Andrews mechanism, it should have left behind a trailing Rayleigh signature. In order to look for signs of a trailing Rayleigh signature, let us select a snapshot of velocity fields at a time corresponding to the arrival of a signal traveling at the Rayleigh wave speed at approximately the center of the field of view, $x_1 = 7$ mm. An estimate of this arrival time is easily obtained as $t = c_R^{\mathrm{HSR}}/d = 67.5$ μs, where $c_R^{\mathrm{HSR}} = 1.18$ km/s is the high strain rate Rayleigh wave speed and $d = (d_{\mathrm{FOV}}+7)$ mm is the distance from the nucleation site to a location set at $x_1 = 7$ mm inside the field of view, where $d_{\mathrm{FOV}} = 72.5$ mm is the distance of the lower end of the field of view ($x_1 = 0$ mm) from the nucleation location. A snapshot of the fault-parallel and fault-normal velocity components at the time $t = 67.6$ μs, the closest time in our record to the estimated one, is shown in Figure 6. The fault-normal velocity exhibits a distinctive peanut-shaped region of negative motion (Figure 6b) like the one seen before for a typical sub-Rayleigh rupture (Figure 5a). However, the fault-parallel velocity field is nearly uniform (Figure 6a), indicating steady state sliding at the back of the rupture. This points toward a disturbance traveling at Rayleigh speeds but without carrying any (or with very small) slip, which implies that there were no well-developed initially sub-Rayleigh rupture, and the rupture either initiated as supershear or transitioned to supershear speeds immediately after nucleation. This result is also confirmed by the fact that the arrival time of the supershear rupture, traveling at an average speed of $V_r = 2.28$ km/s, at the beginning of the field of view $t = d_{\mathrm{FOV}}/V_r \sim 31.7$ μs, is consistent with the rupture traveling at a constant speed of $V_r = 2.28$ km/s since its initiation. Traveling at a lower, sub-Rayleigh speed before transitioning to supershear would have resulted in a later arrival time.

3.2. Supershear Rupture Propagating at $V_r \sim \sqrt{2}c_s^{\mathrm{HSR}}$

Let us now consider another experimental rupture, produced with an applied load of $P = 4.5$ MPa and an inclination angle of $\alpha = 29°$. The resolved normal and shear prestress in this case are $\sigma_0 = P\cos^2\alpha = 3.5$ and $\tau_0 = P\sin\alpha\cos\alpha = 1.9$ MPa, respectively, and also result in a supershear rupture (Figures 3c, 7a, and 7b). This prestress configuration is at the limit between producing a sub-Rayleigh and a supershear rupture (Lu et al., 2010), as the comparatively lower compressive loading promotes sub-Rayleigh ruptures but the

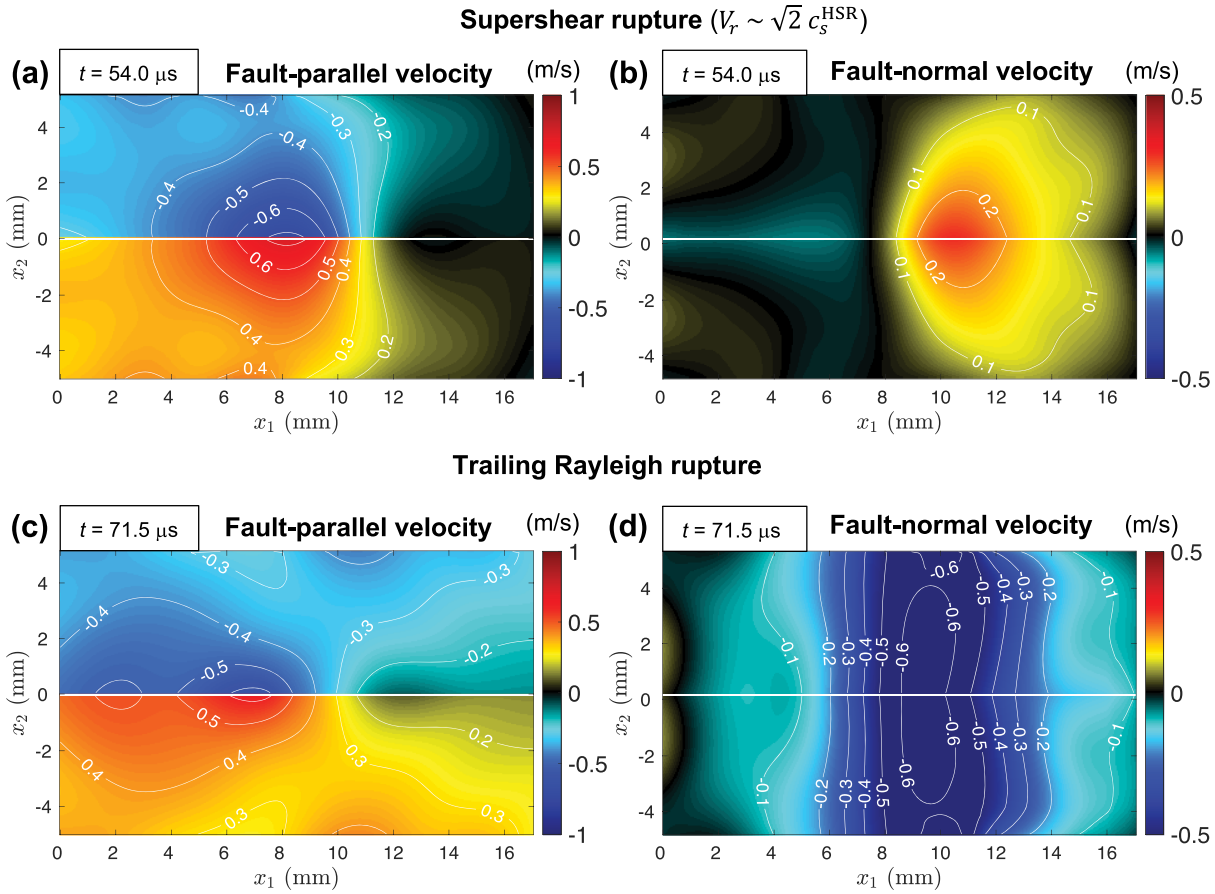

Figure 7. Fault-parallel (left) and fault-normal (right) velocity maps for a supershear rupture (propagating at $V_r \sim \sqrt{2}c_s^{HSR}$) followed by a trailing Rayleigh slip disturbance, obtained for the experimental configuration of $P = 4.5$ MPa and $\alpha = 29°$. The maps are given at two different times after rupture initiation showing (a, b) the initial supershear rupture at $t = 54$ μs and (c, d) the trailing Rayleigh rupture at $t = 71.5$ μs. Note that the trailing Rayleigh rupture (bottom) has a similar velocity pattern to the sub-Rayleigh rupture shown in Figures 4a and 5a.

relatively high nondimensional prestress $\tau_0/\sigma_0 = \tan\alpha = 0.55$ promotes supershear ruptures. Hence, the result is a special type of supershear rupture, propagating at V_r~1.90 km/s (Figure 3c), just above the characteristic Eshelby speed of $\sqrt{2}c_s^{HSR} = 1.81$ km/s (Figure 3c). As mentioned above, according to theoretical predictions the shear Mach features vanish for ruptures propagating at $V_r \sim \sqrt{2}c_s^{HSR}$ (Freund 1998; Mello et al., 2010; Mello et al., 2016). Indeed, the fault-parallel velocity field does not display any Mach features (Figure 7a), in contrast with the corresponding field of the supershear rupture propagating at $V_r = 2.28$ km/s (Figures 2c and 4b). The fault-normal velocity field features a region of positive motion, just ahead of the rupture tip (Figure 7b), without the wedges of negative fault-normal motion aligned with the Mach features seen for the case of faster supershear rupture (Figure 5b).

Regarding the supershear transition mechanism, we observe that after the main supershear rupture has traversed the field of view, the interface nearly locks and then we find a series of snapshots with a distinctive Rayleigh signature in the fault-normal component going across the field of view. For example, at a time of $t = 71.5$ μs after initiation, the fault-normal velocity (Figure 7d) has a similar pattern as that observed before for a sub-Rayleigh rupture (Figure 5a) or for a Rayleigh wave (Figure 6b). Most importantly, the fault-parallel velocity (Figure 7c) indicates the presence of a distinct rupture passing by after the interface nearly locked, with a pattern resembling that is seen earlier for the sub-Rayleigh rupture (Figure 4a). These findings show that the trailing signature is indeed a slip disturbance and is a strong indication that the sub-Rayleigh to supershear transition occurred by the Burridge-Andrews mechanism. Tracking this secondary rupture tip along the interface reveals a propagation speed of 1.16 km/s, which is just below the Rayleigh wave speed $c_R^{HSR} = 1.19$ km/s (Figure 3c). The analysis of the arrival times of the main supershear and trailing

Rayleigh ruptures conducted in section 4.2 confirms that the supershear rupture must have been nucleated as a sub-Rayleigh rupture, subsequently transitioned to supershear speeds, and left a trailing Rayleigh rupture in its wake (Figure 3d).

3.3. Comparison of the Experimentally Produced Velocity Magnitude Fields to Numerical Simulations

To compare the full-field velocities obtained from our experimental measurements to those obtained from numerical simulation, the velocity magnitude fields $|\dot{\mathbf{u}}| = \sqrt{\dot{u}_1^2 + \dot{u}_2^2}$ obtained for the ruptures discussed above in sections 3.1 and 3.2 are plotted next to corresponding plots produced by the linear elastic finite element simulations of Mello et al. (2010) and Mello et al., 2016 (Figure 8). The numerical simulations were produced employing a linear slip-weakening friction law, using a commercial finite element code, ABAQUS (Dessault Systèms Inc.). The velocity magnitude plots are overlaid with a normalized velocity vector plot. To facilitate visualization of the direction of the velocity field, the vector plot is normalized as $\bar{\dot{\mathbf{u}}}=\dot{\mathbf{u}}/|\dot{\mathbf{u}}|$, so that the unit vectors of Figure 8 only carry information about the direction of the velocity field but not its magnitude, which in turn is shown by the color map. The plots are produced for the three rupture speed regimes: (i) sub-Rayleigh $V_r<c_R^{\mathrm{HSR}}$ (Figures 8a and 8b), (ii) supershear with $\sqrt{2}c_s^{\mathrm{HSR}}<V_r<c_p^{\mathrm{HSR}}$ (Figures 8c and 8d), and (iii) supershear with $V_r\sim\sqrt{2}c_s^{\mathrm{HSR}}$ (Figures 8e and 8f). In all three cases, there is a good agreement between the measurements and the numerical simulations. These full-field plots confirm key characteristics of dynamic ruptures in each speed regime that we have analyzed above. The velocity field of the sub-Rayleigh rupture (Figures 8a and 8b) is characterized by a peanut-like shape, mostly dominated by the fault-normal component, as shown by the direction of the velocity vector. The velocity field of the supershear rupture with $\sqrt{2}c_s^{\mathrm{HSR}}<V_r<c_p^{\mathrm{HSR}}$ is characterized by distinct shear Mach fronts associated with the supershear propagation (e.g., Mello et al., 2010; Mello et al., 2016). The velocity magnitude field is dominated by the fault-parallel component, in sharp contrast with the sub-Rayleigh case. When the rupture propagates at $V_r\sim\sqrt{2}c_s^{\mathrm{HSR}}$, the Mach front is expected to vanish (Mello et al., 2010). This is indeed the case for the numerical simulation which propagates at $V_r = \sqrt{2}c_s$ and for the experimental rupture which propagates at a speed just above $\sqrt{2}c_s^{\mathrm{HSR}}$. Although the fault-parallel component still dominates the velocity magnitude, the fault-normal component is comparatively larger than it is for the faster supershear rupture. Note the remarkable similarities of the velocity fields between experiments and simulations for the field of view shown in Figure 8 , despite the fact that the finite element simulations of Mello et al. (2010) and Mello et al. (2016) assume a linear elastic solid, while our experimental measurements are performed on a viscoelastic solid, with high strain rate sensitivity (Gori et al., 2018; Rubino et al., 2017, 2019). In our previous work, we have shown that the formation of pressure shock fronts is most evident when plotting field quantities that are more sensitive to dilatation/compression, such as the volumetric strain rate (Gori et al., 2018), in which case the difference between viscoelastic measurements and linear elastic finite element simulations becomes apparent. On the other hand, the differences in the velocity behavior are more pronounced when zooming out to a larger field of view where the numerical simulations show an expanding dilatational field while the experimental measurements show the formation of the pressure shock fronts (Gori et al., 2018).

4. Temporal Characteristics of Dynamic Ruptures Inferred From Full-Field Measurements

We now focus on analyzing the temporal evolution of the velocity fields. To understand how the fault-parallel and fault-normal components compare to each other for the different rupture speed regimes analyzed so far, we plot their time histories for a point at the center of the field of view ($x_1 = 9.3$ mm) both on the fault ($x_2 = 0^-$) and at distance from it ($x_2 = -5.2$ mm), in Figures 9 and 10. Dashed lines labeled as t_p, t_s, and t_R are plotted in Figures 9 and 10 to indicate the estimated arrival times of the high strain rate pressure and shear and Rayleigh waves at the measurement location, respectively.

4.1. Comparison Between the Fault-Parallel and Fault-Normal Velocity Components of Sub-Rayleigh and Supershear Rupture With $V_r>\sqrt{2}c_s^{\mathrm{HSR}}$

One prominent difference between the velocity time histories of the sub-Rayleigh and supershear rupture (with $V_r>\sqrt{2}c_s^{\mathrm{HSR}}$) is that the sub-Rayleigh rupture has the fault-normal component dominating over the

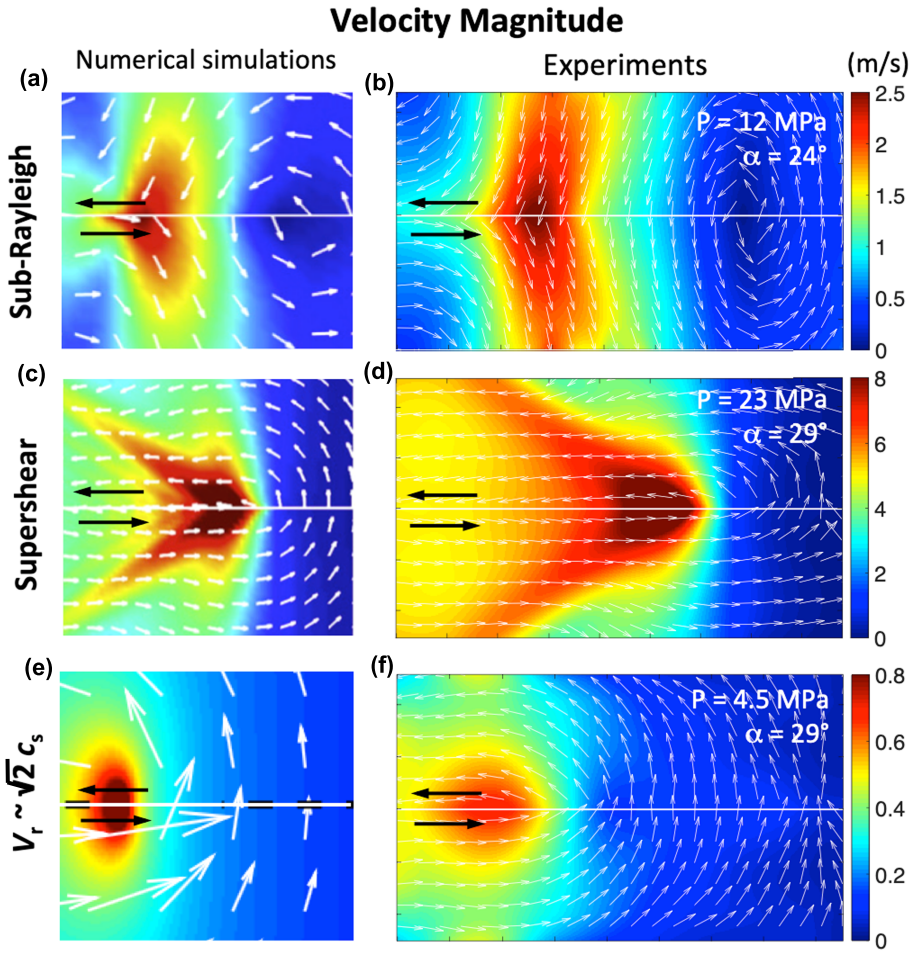

Figure 8. Comparison between the full-field velocity magnitude captured by previous numerical simulations (left) and by our experimental measurements (right). (a, b) Sub-Rayleigh ruptures ($V_r < c_R^{HSR}$); (c, d) supershear ruptures with $V_r > \sqrt{2}\, c_s^{HSR}$; (e, f) supershear ruptures with $V_r \sim \sqrt{2}\, c_s^{HSR}$. The numerical simulations of (a) and (b) are modified from Mello et al. (2010), and that of (e) is modified from Mello et al. (2016). A normalized vector plot is overlaid to show the direction of the velocity vector. These plots indicate that the sub-Rayleigh rupture is dominated by fault-normal motion, while supershear ruptures are governed by fault-parallel motion.

fault-parallel (Figures 9a–9c), while the supershear rupture is characterized by the predominance of the fault-parallel velocity component over the fault normal, consistent with previous measurements and numerical simulations (e.g., Aagaard & Heaton, 2004; Mello et al., 2010). For the sub-Rayleigh rupture, another important characteristic of the fault-parallel velocity time histories is the presence of a pronounced peak (of ~1.2 m/s for this particular rupture) for the trace at $x_2 = 0^-$mm, right at the interface (Figure 9a), and two lower peaks for the trace at $x_2 = -5.2$ mm, which is some distance away from the interface (Figure 9c). The peak of the velocity trace obtained next to the fault ($x_2 = 0^-$mm) is due to the near-tip region of the rupture, while the presence of an additional peak in the off-fault measurement ($x_2 = -5.2$ mm) is associated with the dilatational field extending ahead of the rupture tip. The fault-normal velocity of the sub-Rayleigh rupture is characterized by a small positive motion, ahead of the rupture tip, followed by a more pronounced negative, downward, motion with a peak of ~2.3 m/s (Figure 9a). This signal only mildly attenuates off fault, in the near field, the negative peak being at around ~1.9 m/s at $x_2 = -5.2$ mm (Figure 9b and section 5). However, it is expected to attenuate more appreciably in the far field (Freund, 1998; Mello et al., 2016). These individual measurements are better understood using the full-field map of Figure 2b, where an elongated shape of negative motion appears in the direction perpendicular to the fault and does not attenuate significantly within the field of view (see section 5). The fault-parallel velocity of the supershear field measured next to the fault (at $x_2 = 0^-$mm) is

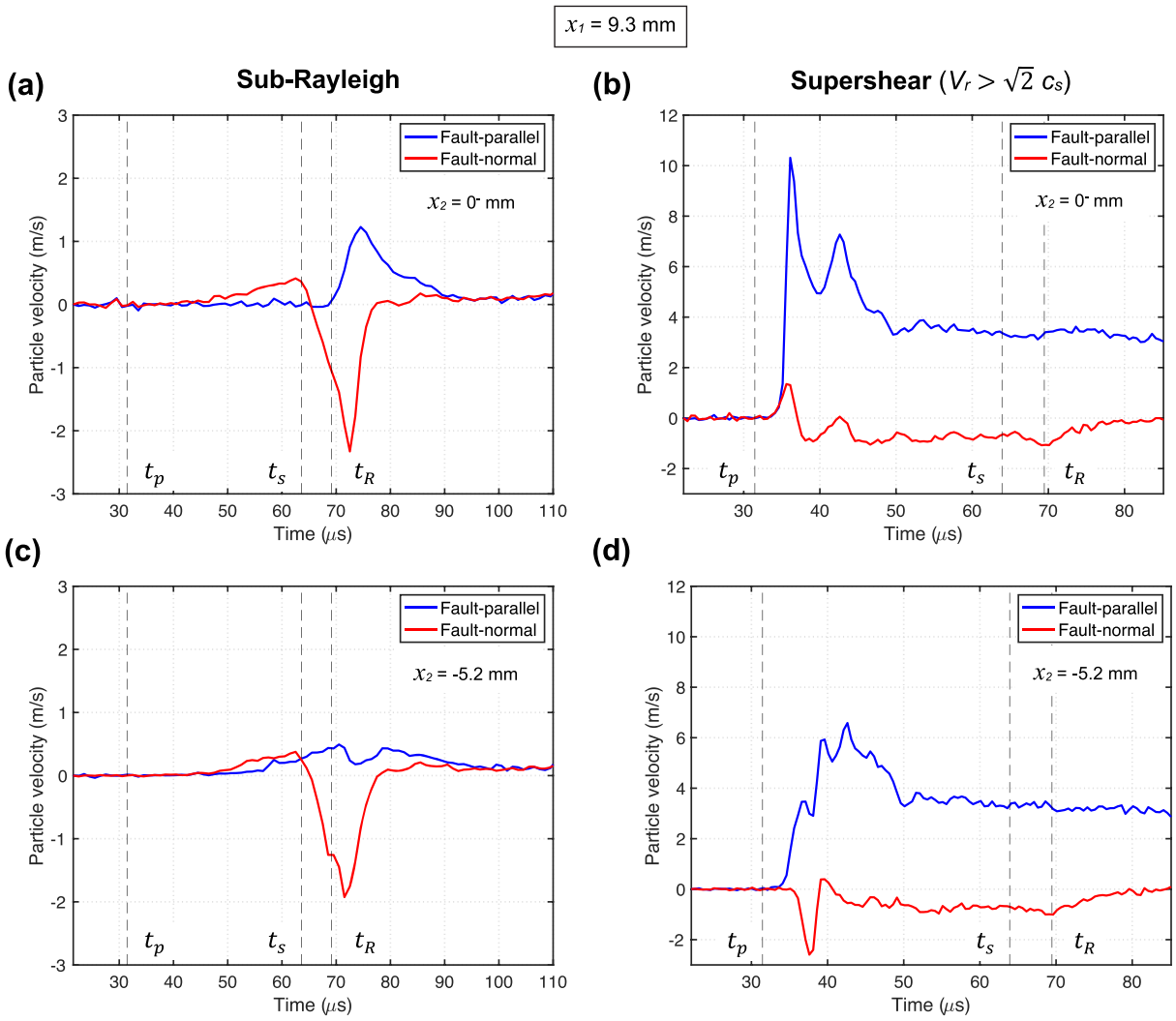

Figure 9. Particle velocity time histories for the sub-Rayleigh (left) and supershear (right) ruptures of Figure 2. (a, b) On-fault ($x_1 = 0^-$) and (c, d) off-fault ($x_1 = -5.2$ mm) time histories obtained at a distance of 81.1 mm from the nucleation site ($x_1 = 8.9$ mm). Dashed lines marked with t_p, t_s, and t_R indicate the arrival times of *P*, *S*, and Rayleigh waves. The sub-Rayleigh rupture arrives together with the Rayleigh waves, while the supershear rupture is well ahead of the shear waves, as it approaches the pressure wave speed. The velocity traces reveal that the fault-normal component is dominant for the sub-Rayleigh rupture, but the fault-parallel component governs the supershear rupture motion.

characterized by an initial sharp peak, exceeding 10 m/s, followed by a second peak (Figure 9b). The second peak is likely due to the finite thickness of the specimen and has been attributed to the reflection of the shear shock front at the rear face of the specimen (Lu et al., 2010; Mello et al., 2010; Rubino et al., 2017, 2019). In the off-fault trace (at $x_2 = -5.2$ mm), another peak develops ahead of those associated to the shear motion, and it is associated to the dilatational field (Figure 9d), similarly to the case of the sub-Rayleigh rupture. The fault-normal velocity time history of the supershear rupture exhibits a prominent positive peak for the measurement at $x_2 = 0^-$mm (Figure 9b), and a prominent negative peak for the measurement at $x_2 = -5.2$ mm (Figure 9b), reflecting the full-field structure shown in Figure 5b. The negative peak in the off-fault measurement is followed by a smaller positive peak, corresponding to the two symmetric narrow wedges visible in Figure 5b and a nearly constant level of negative velocity associated to the central wedge shown in Figure 5b. Note that while the positive peak present in the near-fault region disappears almost immediately away from the fault, the negative motion, associated to the shock fronts, is carried at a much larger distances from the fault, as it will also be shown in section 4.3. The velocity time histories shown in Figure 9 also reveal that the sub-Rayleigh rupture mode is pulselike, that is, particle

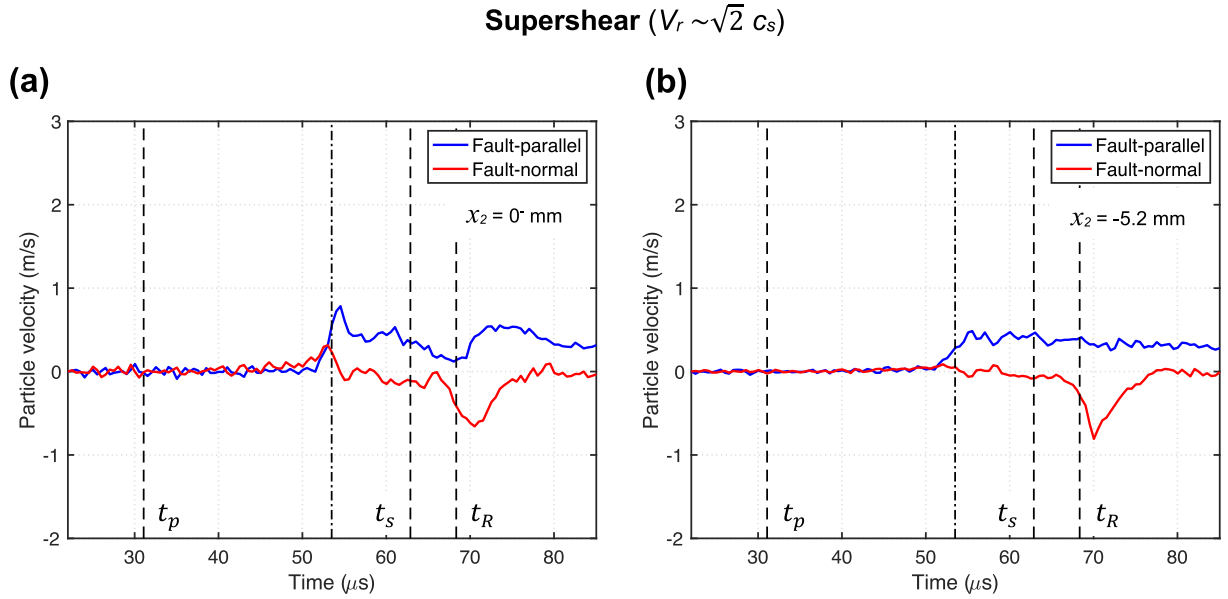

Figure 10. Particle velocity time histories for a supershear ruptures traveling at $V_r \sim \sqrt{2}\, c_s^{HSR}$. (a) On-fault ($x_2 = 0^-$) and (c, d) off-fault ($x_2 = -5.2$ mm) velocity time histories obtained at a distance of 81.9 mm from the nucleation site ($x_1 = 8.6$ mm). Dashed lines marked with t_p, t_s, and t_R indicate the arrival times of the high strain rate *P*, *S*, and Rayleigh waves. The dashed-dotted line represents the arrival time of a signal traveling exactly at $\sqrt{2}\, c_s^{HSR}$, initiated at a distance *L* (see equation (3) and Figure 3d) from the main rupture nucleation location. The actual rupture arrives just ahead of it, indicating that it is traveling at a speed just above $\sqrt{2}\, c_s^{HSR}$, as confirmed by the rupture speed plot (Figure 3c).

velocity and associated slip rate go to zero behind the rupture tip, while the supershear rupture behaves as a cracklike rupture, with the particle velocity retaining a nonzero level behind the rupture tip. Separate experiments producing sub-Rayleigh crack-like ruptures (not shown here), conducted with a lower prestress and larger inclination angle than those considered here (e.g., $P = 4$ MPa and $\alpha = 29°$), reveal that while the fault-parallel particle velocity becomes low but nonzero behind the rupture tip, the fault-normal velocity exhibits the same characteristics described for the sub-Rayleigh pulse.

4.2. Velocity Time Histories of a Supershear Rupture Propagating at $V_r \sim \sqrt{2} c_s^{HSR}$

Let us now analyze the velocity time histories for the case of the supershear rupture propagating at $V_r \sim; \sqrt{2}\, c_s^{HSR}$. In this case, unlike for the case of the previous supershear rupture, the transition to supershear speeds leaves a trailing Rayleigh rupture (Figure 7). The particle velocities time histories reveal first the arrival of the leading supershear rupture at $t \sim 52$ μs, marked by the fault-parallel velocity signal dominating over the fault-normal component (Figure 10) and later the arrival of the trailing Rayleigh rupture at $t \sim 70$ μs, characterized by a predominant fault-normal signal, as seen for a typical sub-Rayleigh rupture (Figures 9a and 9c).

The average speed of the leading supershear rupture is $V_r = 1.90$ km/s, roughly 8% higher than $\sqrt{2} c_s^{HSR}$, corresponding to an arrival time of $t = 37.2$ μs if the rupture propagated at this constant speed from the beginning. Instead, the arrival time of this rupture at the measuring location at a distance of $d_{meas} = 91.3$ mm from the nucleation site is $t = 52.3$ μs (Figure 10a), which indicates that the rupture must have traveled at a lower, sub-Rayleigh speed before transitioning to supershear. We can use the arrival times of the supershear and the trailing Rayleigh ruptures to compute the approximate sub-Rayleigh to supershear transition distance *L*, assuming a constant propagation at each speed regime and a seamless transition of the rupture tip from sub-Rayleigh to supershear speed.

Considering the main rupture traveling at a sub-Rayleigh speed V_{SR} until it transitions to supershear speed at a time t_{tran}, and subsequently traveling at V_{SS}, for a time t_{SS}, until it reaches the measuring location $d = 81.1$ mm of Figure 10a, yields

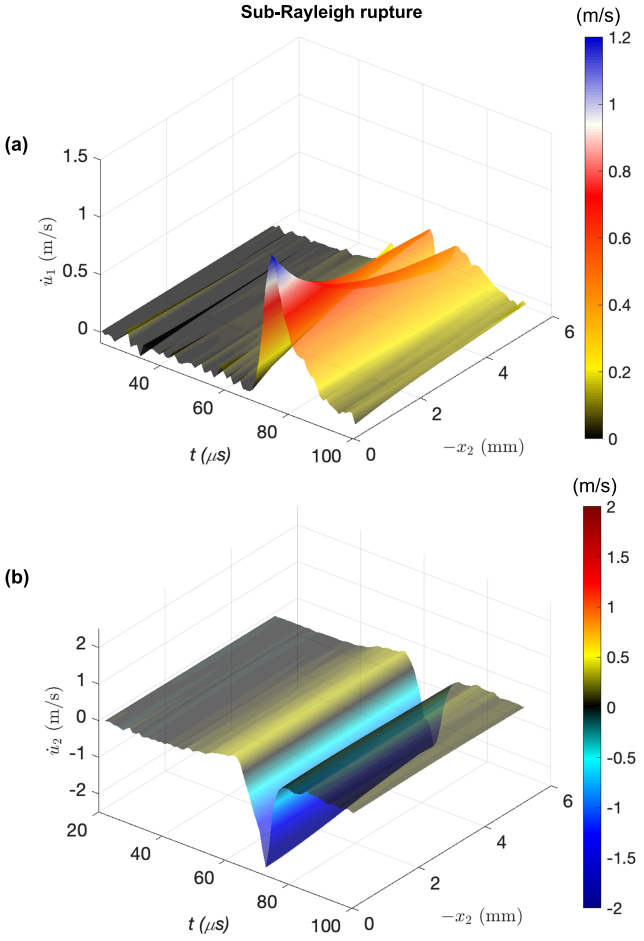

Figure 11. Spatiotemporal plots for the sub-Rayleigh rupture. (a) Fault-parallel and (b) fault-normal particle velocities plotted against time and position along the (negative) x_2 axis. The temporal history of the fault-parallel component features one peak on the interface and two peaks at a distance from the fault. The fault-normal component is characterized by one peak, which mildly attenuates in the near field.

$$d = V_{SR} t_{tran} + V_{ss} t_{SS} \tag{1}$$

where t_{SS} is given by

$$t_{SS} = t_{SS} - t_{tran} \tag{2}$$

$t_{SS} = 52.3$ μs is the arrival time of the supershear rupture. The time t_{tran} taken for the rupture to transition to supershear speeds can be computed from equations (1) and (2). The transition distance L is then given by $L = V_{SR} t_{tran}$ or

$$L = V_{SR} \frac{V_{SS} t_{SS} - d}{V_{SS} - V_{SR}} \tag{3}$$

Using the measured speeds $V_{SS} = 1.90$ and $V_{SR} = V_{TR} = 1.16$ km/s, where V_{TR} is the speed of the trailing Rayleigh rupture, equation (3) yields $L = 28.8$ mm. Note that equation (3) can equivalently be obtained by the following relation:

$$t_{SS} = \frac{L}{V_{SR}} + \frac{d - L}{V_{SS}} \tag{4}$$

We can use the transition distance to compute the arrival time at the location $d_{meas} = 81.1$ mm of a signal initially traveling at the sub-Rayleigh speed $V_{SR} = 1.16$ km/s up to the transition distance L and then propagating exactly at $\sqrt{2} c_s^{HSR}$, in order to compare it with the present rupture. Writing an equation similar to equation (4) with $\sqrt{2} c_s^{HSR}$ at denominator of the second addendum, we get $t_{sq2} = 53.5$ μs. This arrival time is represented as a dashed-dotted line in Figure 10 and indicates that the leading supershear rupture arrives just a few microseconds earlier, consistent with it propagating just above $\sqrt{2}\, c_s^{HSR}$ as determined independently by tracking the rupture tip position along the interface.

4.3. Spatiotemporal Properties of Sub-Rayleigh and Supershear Ruptures

The spatial and temporal characteristics that so far we have analyzed separately for simplicity can be summarized in spatiotemporal plots where the velocity components are plotted versus time and versus distance (Figures 11 and 12). These results reveal how the fault-parallel velocity peak present on the interface of the sub-Rayleigh rupture morphs into a double peak off fault (Figure 11a) and indicate a mild attenuation of the fault-normal velocity in the near-field region (Figure 11b). For the supershear rupture, Figure 12a reveals the initial attenuation of the main rupture peak in the immediate vicinity of the fault (~2 mm) but a near-constant level thereafter. Figure 12b shows how the positive fault-normal velocity peak at the interface attenuates rapidly, as this peak corresponds to region of positive motion concentrated around the interface (Figures 3d and 5b). On the other hand, a pronounced negative peak, not present in the on-fault time history, appears off fault and propagates unattenuated, as it is associated with the shear shock front. To better illustrate the spatiotemporal features of the studied ruptures, an animated version of the figures discussed in this section is given in the supporting information (Movies S3 and S4) for the supershear case. Note that while our results are fully consistent with the previous velocimeter measurements (Mello et al., 2010; Mello et al., 2016), such evolution of the off-fault fields can only be revealed by the full-field dynamic measurements presented here.

5. Amplitude Decay of the Velocity Fields

The spatiotemporal plots (Figures 11 and 12) already provide an insight into the amplitude decay of the velocity fields. To facilitate the study of the velocity attenuation with distance from the fault, let us consider

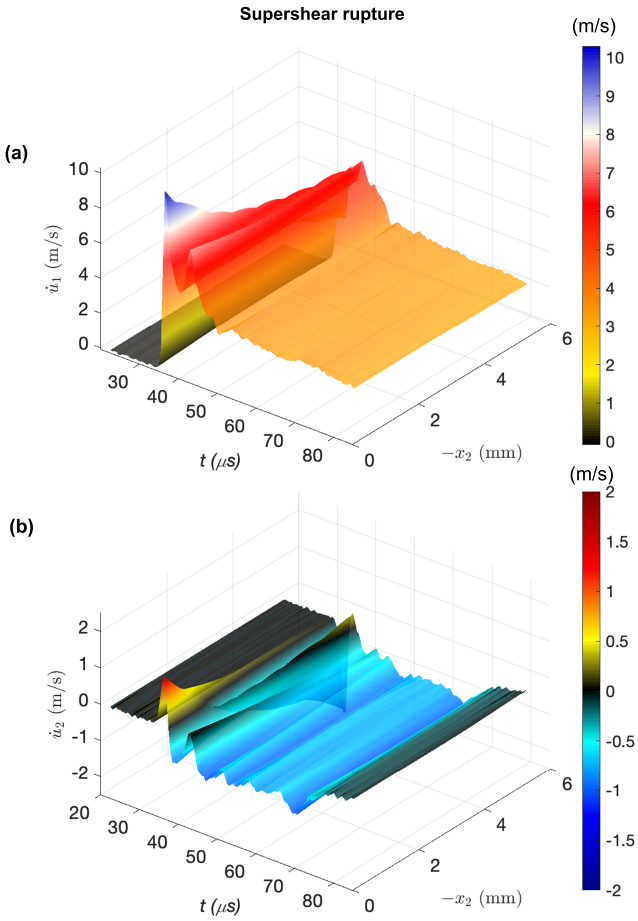

Figure 12. Spatiotemporal plots for the supershear rupture. (a) Fault-parallel and (b) fault-normal particle velocities plotted against time and position along the (negative) x_2 axis. After a rapid attenuation in the first ~2 mm the main supershear peak propagates away from the fault with little attenuation. The fault-normal component has a larger positive peak followed by a smaller negative one near the fault. The positive peak disappears away from the fault, but a pronounced negative peak associated with the shock fronts appears propagating a strong signal at larger distances form the fault.

velocity seismograms produced at a fixed x_1 and discrete values of increasing x_2 (Figure 13), similar to the synthetic seismograms of Dunham and Bhat (2008).

The seismograms corresponding to the sub-Rayleigh and supershear ($V_r > \sqrt{2}c_s^{\mathrm{HSR}}$) ruptures discussed in sections 3 and 4 are produced at $x_1 = 8.6$ mm and at selected values of x_2, starting at the pixel immediately below the interface and then every 10 pixels or ~0.46 mm in the negative x_2 direction (Figures 13a and 13b and 13c and 13d, respectively). These two ruptures are imaged with a field of view of 19 × 12 mm^2, depicted in Figure 1, which offers a dense spatial coverage in the near field. In order to study the far-field behavior of a supershear rupture ($V_r > \sqrt{2}c_s^{\mathrm{HSR}}$), we conduct another experiment using similar loading and geometry configuration ($P = 25$ MPa and $\alpha = 29°$) as for the previous experiment ($P = 23$ MPa and $\alpha = 29°$) and we employ a larger field of view: 131 × 82 mm^2. More details about the dynamic rupture captured with the larger field of view can be found in our previous study (Rubino et al., 2019). The seismograms are produced at $x_1 = 62$ mm and at selected values of x_2, starting at the pixel immediately below the interface and then every 10 pixels or ~3.28 mm in the negative x_2 direction (Figures 13e and 13f). The arrival times of the high strain rate p, s, and Rayleigh waves are marked in the seismograms as dashed lines and are computed as $t_w = \sqrt{x_1^2 + x_2^2}/c_w$, where $w = p, s, R$, for the p, s, and Rayleigh waves, respectively. Note that as $x_2 \to 0$, the arrival times tend to the vertical lines $t_w \sim x_1/c_w$ in the seismograms produced in the near field (Figures 13a–13d). As x_2 becomes larger the fronts become curved, as apparent from the seismograms produced for the large field of view (Figures 13e and 13f).

The velocity patterns shown in the seismograms of Figure 13 are by and large in agreement with those exhibited by the numerical simulations of Dunham and Bhat (2008), including the persistence of the fault-parallel motion at increasing distance from the fault for the supershear cases and the persistence of the fault-normal motion in the near field for sub-Rayleigh ruptures. In order to more accurately compare our measurements with their simulations, let us consider the same nondimensional quantities for velocity, time, and distance from the interface, as defined in Dunham and Bhat (2008). The nondimensional velocity is defined as $\overline{V}_i = V_i\,\mu/c_s\sigma_{12}$, where $V_i = \dot{u}_i$ is the particle velocity, μ is the shear modulus, c_s the shear wave speed, and σ_{12} the shear stress drop; the nondimensional time as $\bar{t} = c_s t/w$, where t is time and w the fault thickness; and the nondimensional distance from the interface as $\bar{x}_2 = x_2/w$. Let us compare some typical values of our measurements of fault-parallel velocity to the simulations of Dunham and Bhat (2008). Our ruptures have peak particle velocities on the order of $V_1 = 1 - 10$ m/s, and dynamic stress drops of $\sigma_{12} = 2 - 8$ MPa, with the opposite ends of the range corresponding to the sub-Rayleigh and supershear ruptures of Figures 13a and 13c, respectively. The shear stress evolution for these two ruptures is not shown here, but it is given in Rubino et al. (2017). Taking $\mu = 1.96$ GPa and $c_s = c_s^{\mathrm{HSR}} = 1,280$ m/s, as the dynamic shear modulus and shear wave speed (Mello et al., 2014; 2016; Rubino et al., 2017), and $t \sim 100$ μs as characteristic observation time window yields $\bar{t} \sim 13$ and $\overline{V}_1 = 0.76–1.9$, for the sub-Rayleigh and supershear ruptures, respectively, which is on the same order of magnitude as the values reported in Dunham and Bhat (2008). The fault geometry of Dunham and Bhat (2008) features a strike-slip fault breaking the surface and locked at depth. They use the fault width w as a normalizing length scale. In the experimental ruptures discussed here, we take the plate thickness $h = 10$ mm as the length scale to nondimensionalize the distance from the fault. Note that the two length scales w and h are physically different, and in particular that having the lower end of the fault locked plays a

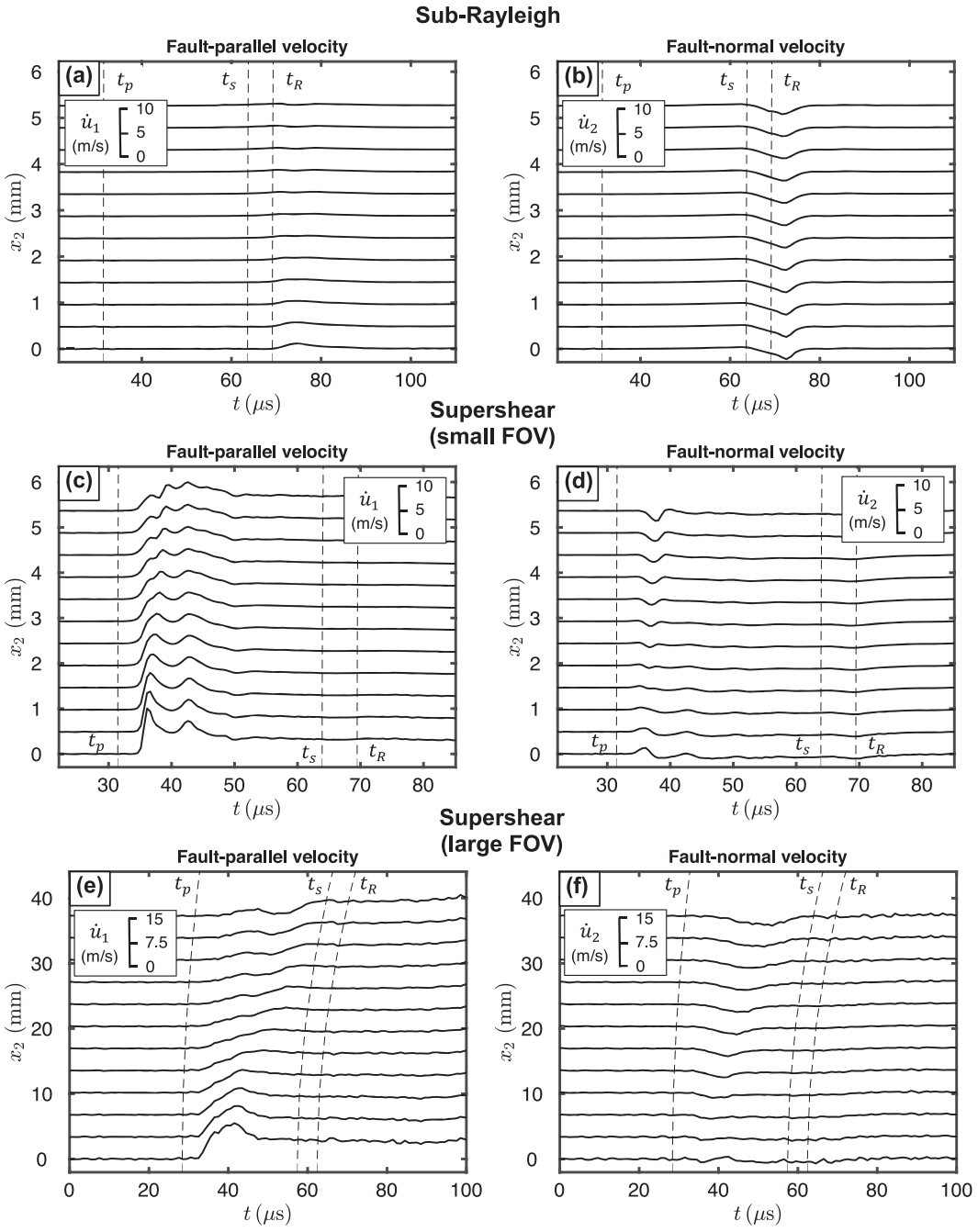

Figure 13. Velocity seismograms for the sub-Rayleigh (a, b) and supershear, (c, d) and (e, f) ruptures produced at fixed x_1 and varying x_2. The sub-Rayleigh (top panels) and supershear (central panels) ruptures are captured by a field of view (FOV) of 19×12 mm^2 (Figure 1). The seismograms of the bottom panels are associated with another supershear rupture, captured by a larger field of view, 131×82 mm^2. The arrival of the pressure, shear, and Rayleigh wave fronts is marked by dashed lines labeled as t_p, t_s, and t_R, respectively.

key role during rupture propagation, sending arrest waves to the propagating rupture. The nondimensional distances from the fault for the simulations of Dunham and Bhat (2008) are reported up to $x_2/w = 15$, and therefore, they are suitable to study the attenuation and far-field rupture behavior. On the other hand, the nondimensional distance from the fault for the ruptures of Figures 13a and 13b and 13c and 13d, which are analyzed with a small field of view of 19×12 mm^2, is only $\bar{x}_2^{\max} = x_2^{\max}/h = 0.5$. This suggests that the fields captured by this imaging window are

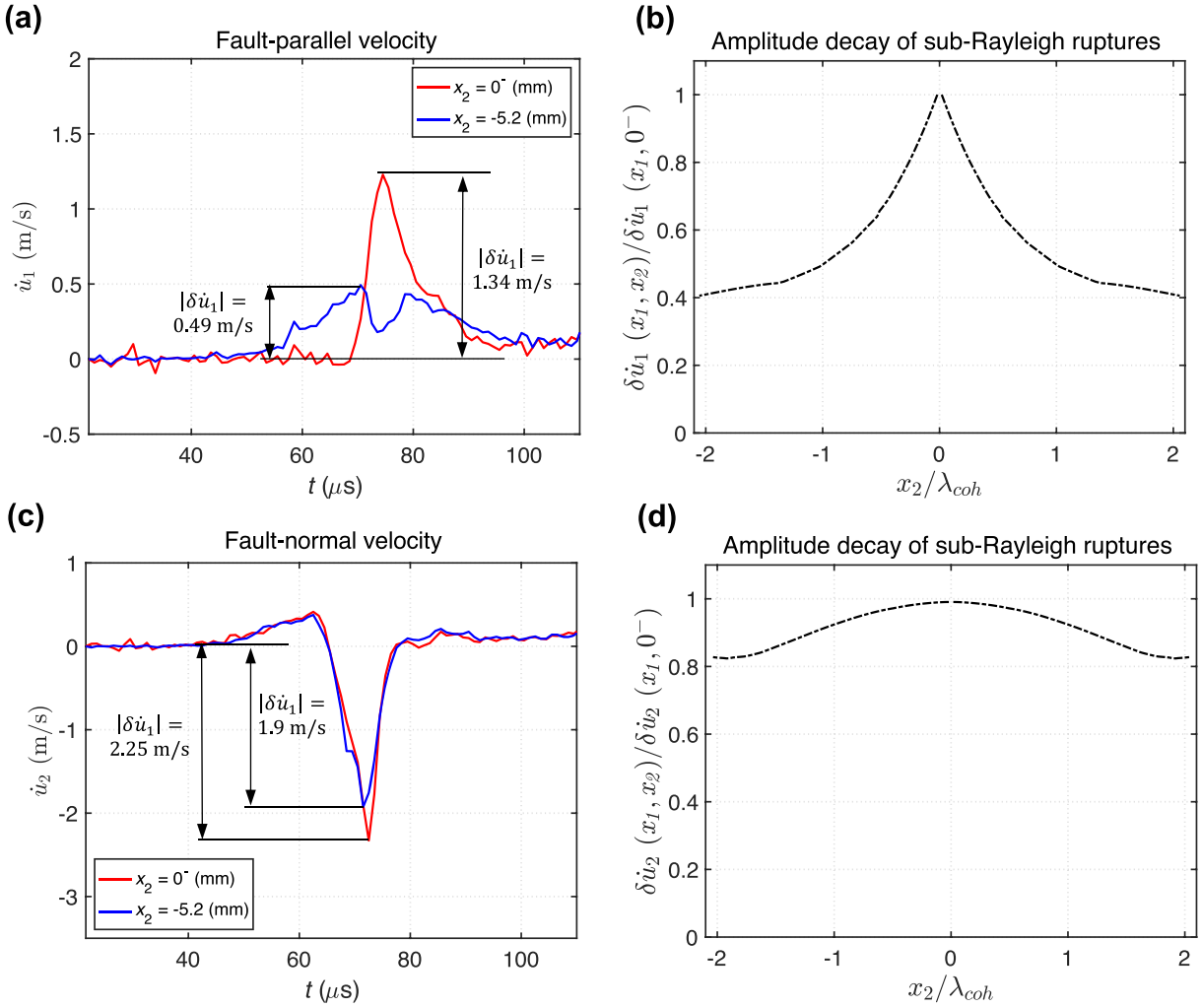

Figure 14. Amplitude decay of sub-Rayleigh ruptures, at $x_1 = 8.9$ mm. (a, c) Fault-parallel and fault-normal particle velocity time histories at two distances from the fault. The figure shows the peaks tracked to study the amplitude decay. (b, d) Amplitude decay of the particle velocity peaks. The distance from the fault is normalized by the cohesive zone size, computed as detailed in the text. Note that the fault-normal velocity does not attenuate as $1/\sqrt{r}$, with distance from the rupture tip r, for distances comparable to the cohesive zone size where the asymptotic solution does not hold.

appropriate to describe the near-field behavior but not the attenuation characteristics. The larger field of view of 131 × 82 mm^2 gives $\bar{x}_2^{\max} = x_2^{\max}/h = 4$ and can be used to describe some features of the far-field behavior.

According to theoretical predictions of singular crack solutions, the particle velocities of a sub-Rayleigh rupture should decay as $1/\sqrt{r}$ where r is the distance from the crack tip (Freund, 1998). To verify this, let us analyze further the sub-Rayleigh rupture of Figures 13a and 13b by tracking the particle velocity swings $\delta\dot{u}_1$ and $\delta\dot{u}_2$ of the particle velocity time histories as they evolve away from the fault at a fixed value of x_1, as shown in Figures 14a and 14b, and 14c and 14d for $\delta\dot{u}_1$ and $\delta\dot{u}_2$, respectively. The particle velocity swings $\delta\dot{u}_i(x_1, x_2)$, where i = 1,2, are normalized in Figures 14b and 14d by the corresponding value at $x_2 = 0^+$, $\delta\dot{u}_i(x_1, 0^+)$. The fault-parallel velocity seems to attenuate roughly with $1/\sqrt{r}$. However, this is not the case for the fault-normal velocity, which decays very mildly with r. The singular crack solution is valid at a distance from the crack tip several times larger than the cohesive zone size λ_{coh}. We can measure the cohesive zone size by computing the shear stress along the interface and determining the length scale over which the shear stress decreases from its peak to the residual level. Using the shear stress reported in Rubino et al. (2017) for the same ruptures as those analyzed here, we determine that our ruptures have a cohesive zone size of λ_{coh} ~2.5 mm, and consequently with the imaging

windows employed here, we are monitoring the particle velocity only up to $\lambda_{coh}/r \sim 2$, that is, too close to the rupture tip for the singular crack solutions to be valid. Nonetheless our measurements showing a more pronounced attenuation of the fault-parallel velocity component compared to the fault-normal are consistent with the theoretical predictions of Mello et al., 2016, based on linear elastic solutions. Our results are also in agreement with the measurements of Mello et al. (2016), whose point-wise measurements obtained with laser velocimeters for $x_2 \leq 3$ mm show very little attenuation of $\delta\dot{u}_2$ (see Figure 18 in Mello et al., 2016). Moreover, our measurements are able to resolve at a much higher level of details features within a cohesive zone size that were not possible to resolve with the previous laser velocimeter measurements.

Let us now turn our attention to study the attenuation of the dilatational field of supershear ruptures. The singular elastic asymptotic solutions for the in-plane particle velocity field of a supershear crack can be decomposed into a shear $\dot{u}_i^s$ and dilatational $\dot{u}_i^d$ component as (Freund, 1998; Mello et al., 2016) $\dot{u}_i = AV_r\left(\dot{u}_i^s + \dot{u}_i^d\right)$, with $i = 1,2$; where $A = K_{II}/\mu$ is an effective dynamic stress intensity factor, K_{II} is the mode II stress intensity factor, μ is the shear modulus, and V_r is the rupture speed. The dilatational velocity field attenuates as (Freund, 1998; Mello et al., 2016) $\dot{u}_i^d \sim 1/r_d^q$, where r_d is given by $r_d = \sqrt{\xi_1^2 + (\alpha_d\xi_2)^2}$, in the local coordinate system (ξ_1, ξ_2), centered at the rupture tip. Note that at the crack tip $\xi_1 = 0$, while $\xi_2 = x_2$ by definition. The coefficient α_d is a function of the rupture speed V_r and the dilatational speed c_d: $\alpha_d = \sqrt{1-(V_r/c_d)^2}$. The exponent q is given by (Freund, 1998; Mello et al., 2016):

$$q = \frac{1}{\pi}\tan^{-1}\left[\frac{4\alpha_d\beta_s}{\left(2-V_r^2/c_s^2\right)^2}\right] \tag{5}$$

where $\beta_s = \sqrt{(V_r/c_s)^2-1}$. Evaluation of equation (4) indicates that $0 \leq q \leq 1/2$ and that q has a maximum value of $q = 1/2$ as $V_r \to \sqrt{2}c_s$, while $q \to 0$ as $V_r \to c_s$ or $V_r \to c_d$. The singularity of the dilatational field of a supershear rupture r_d^{-q} is therefore weaker than that of the particle velocity of a sub-Rayleigh rupture $r^{-1/2}$, which indicates a slower decay of the dilatational field in the far field. As noted above, the $r^{-1/2}$ singularity comes back when $V_r \to \sqrt{2}c_s$. The supershear rupture of Figures 7a and 7b propagates at $V_r \sim 1.90$ km/s and, as we have seen above, approaches the critical speed $\sqrt{2}c_s = 1.81$ km/s. Using the high strain rate wave speeds yields $q = 0.4956$. The imaging window employed for the supershear rupture of Figure 7 does capture the dilatational field; however, it cannot be employed to study its attenuation since it is on the same order of magnitude as the cohesive zone size.

To study the attenuation characteristics of the dilatational field at larger distances from the fault, let us consider the supershear rupture captured by the large field of view (Figures 13e and 13f). That supershear rupture propagates at $V_r = 2.34$ km/s, which yields $q = 0.31$. To track the dilatational field, we start by analyzing the fault-parallel particle velocity time history at $x_1 = 65.5$ and $x_2 = 0^-$ mm; we take the velocity swing $\delta\dot{u}_1^d(x_1, 0^-)$ as the reference value to normalize the velocity swings $\delta\dot{u}_1^d(x_1, x_2)$ for $x_2 < 0$. We then consider the velocity time histories at $x_2 < 0$, while keeping x_1=constant, and track the velocity swings $\delta\dot{u}_1^d(x_1, x_2)$, as shown in Figure 15. The fault-parallel velocity time history tracked at a distance from the fault produces a distinct peak associated to the dilatational field, ahead of the velocity peak associated to the shear field. Since the two peaks coincide at the rupture tip, we track the dilatational field after it forms a distinct peak, at some distance from the fault. The nondimensional dilatational peak $\delta\dot{u}_1^d(x_1, x_2)/\delta\dot{u}_1^d(x_1, 0^-)$ decay with distance from the fault x_2 is shown in Figure 15b. We find that the function $f(x_1, x_2) \sim 1/x_2^q$, with $q = 0.31$ given by equation (4), fits well the experimental data, indicating good agreement between our experimental measurements and the singular crack theory. These are the first experimental measurements to verify the attenuation of the dilatational field. Note that resolving the dilatational field as a function of the distance from the fault using velocimeter measurements would have required multiple experiments since it is only possible to use two to three velocimeters per test. On the other hand, with the current measurements based on DIC, it is possible to characterize the attenuation by only one test.

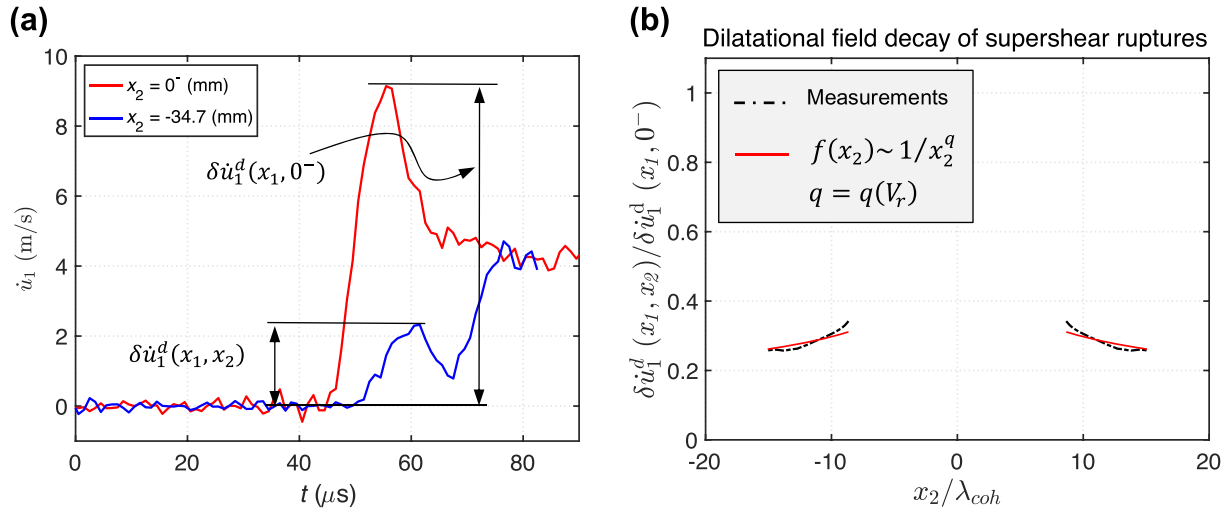

Figure 15. Amplitude decay of dilatational field of supershear ruptures, at $x_1 = 65.5$ mm. (a) Fault-parallel particle velocity time history at two difference distances from the fault. The illustration shows the dilatational peaks tracked to study the amplitude decay on the right panel. (b) Amplitude decay of the dilatational field. The distance from the fault is normalized by the cohesive zone size, computed as detailed in the text. The peak associated with the dilatational field is tracked for distances from the fault $x_2 \geq 20$ mm. For distances $x_2 < 20$ mm, the peak associated with the dilatational and shear fields are indistinguishable as they tend to coalesce at the rupture tip. Note that the dilatational field follows the theoretically predicted decay $1/x_2^q$, where the exponent q is a function of the rupture speed defined by equation (4).

6. Conclusions

We have characterized the spatiotemporal properties of experimental dynamic shear ruptures propagating at sub-Rayleigh and supershear speeds by using the DIC method coupled with ultrahigh-speed photography. Our measurements reveal the full-field structure of the velocity components at a level of spatial and temporal resolution that was unattainable until recently and that approaches that of numerical simulations. Indeed, the velocity maps obtained from our measurements are in excellent qualitative agreement with previous finite element simulations.

We have analyzed three distinct rupture regimes using three experimental ruptures to characterize their properties: a sub-Rayleigh rupture propagating at $V_r < c_R^{\mathrm{HSR}}$, a supershear rupture propagating at $V_r \sim \sqrt{2}\, c_s^{\mathrm{HSR}}$, and a supershear rupture propagating at $V_r > \sqrt{2}\, c_s^{\mathrm{HSR}}$. The full-field maps reveal the marked fault-normal motion of the sub-Rayleigh rupture being persistent in the near field, that is, at distances from the fault within two cohesive zone sizes. The supershear rupture propagating at $V_r > \sqrt{2}\, c_s^{\mathrm{HSR}}$ is characterized by the shear shock fronts both in the fault-parallel and in the fault-normal components. For the particular supershear rupture studied here, the dilatational field develops another set of (pressure) shock fronts that form the leading edge of both velocity fields. The velocity features associated with the shock fronts are carried away at large distances from the fault. There are also features localized in the near field that do not propagate away from the fault, such as the localized positive motion in the fault-normal velocity. The discontinuity features associated with the shock fronts disappear for the supershear rupture propagating at $V_r \sim \sqrt{2}\, c_s^{\mathrm{HSR}}$, as expected from singular elastic solutions. The full-field maps also allow us to clearly identify a trailing Rayleigh rupture propagating in the wake of the leading supershear rupture indicating, together with arrival times and rupture speed analysis, that in this case the sub-Rayleigh to supershear transition occurred through the Burridge-Andrews mechanism. Conversely, the same analysis conducted for the faster supershear rupture ($V_r > \sqrt{2}\, c_s^{\mathrm{HSR}}$) indicates that that rupture may have propagated with similar supershear speeds right from nucleation, likely due to the higher levels of prestress.

The time history traces obtained from the full-field measurements confirm that supershear ruptures are characterized by a more pronounced motion in the fault-parallel direction, while for sub-Rayleigh ruptures the fault-normal velocity predominates, in accordance to previous theoretical and experimental studies. At the same time, our measurements reveal the full-field structure of the velocity components

and help to explain previous spatially sparse velocimeter time histories, only available at a limited number of locations, for example, the transition from one to two peaks in the fault-parallel particle velocity time history of sub-Rayleigh ruptures, the presence of a positive fault-normal velocity in the near-tip field of supershear ruptures, rapidly decaying with distance from the fault, and the appearance of negative fault-normal velocity features, associated with the shock fronts, radiating in the far field.

The full-field maps also allow us to quantify the attenuation characteristics. The small imaging windows used in this study are appropriate to analyze the near-field behavior at distances from the fault comparable to the cohesive zone size, revealing relatively minor attenuation within that region of the fault-normal (but not of the faultparallel) velocity of sub-Rayleigh ruptures. The large imaging window allows us to investigate the rupture behavior at larger distances from the fault, several cohesive zone sizes away. For the supershear rupture analyzed with the large field of view, the amplitude decay of the dilatational field is consistent with the theoretical estimates given by the singular elastic solutions.

Acknowledgments
This study was supported by the U.S. National Science Foundation (NSF) (Grants EAR 1321655 and EAR-1651235), the U.S. Geological Survey (USGS) (Grant G16AP00106), and the Southern California Earthquake Center (SCEC), Contribution 9985. SCEC is funded by NSF Cooperative Agreement EAR-1033462 and USGS Cooperative Agreement G12AC20038. Data sets used in this study are available from the Repository CaltechDATA (https://doi.org/10.22002/d1.1328).

References

Aagaard, B. T., & Heaton, T. H. (2004). Near-source ground motions from simulations of sustained intersonic and supersonic fault ruptures. *Bulletin of the Seismological Society of America*, *94*(6), 2064–2078.
Andrews, D. (1976). Rupture velocity of plane strain shear cracks. *Journal of Geophysical Research*, *81*(32), 5679–5687.
Andrews, D. (2010). Ground motion hazard from supershear rupture. *Tectonophysics*, *493*(3-4), 216–221.
Archuleta, R. J. (1984). A faulting model for the 1979 Imperial Valley earthquake. *Journal of Geophysical Research*, *89*(B6), 4559–4585.
Ayoub, F., Leprince, S., & Keene, L. (2009). *User's guide to COSI-CORR co-registration of optically sensed images and correlation* (Vol. 38). Pasadena, CA, USA: California Institute of Technology.
Bao, H., Ampuero, J.-P., Meng, L., Fielding, E. J., Liang, C., Milliner, C. W., et al. (2019). Early and persistent supershear rupture of the 2018 magnitude 7.5 Palu earthquake. *Nature Geoscience*, *12*(3), 200–205.
Bayart, E., Svetlizky, I., & Fineberg, J. (2016). Slippery but tough: The rapid fracture of lubricated frictional interfaces. *Physical Review Letters*, *116*(19), 194301. https://doi.org/10.1103/PhysRevLett.116.194301
Ben-David, O., Rubinstein, S. M., & Fineberg, J. (2010). Slip-stick and the evolution of frictional strength. *Nature*, *463*(7277), 76–79. https://doi.org/10.1038/nature08676
Ben-Zion, Y. (2001). Dynamic ruptures in recent models of earthquake faults. *Journal of the Mechanics and Physics of Solids*, *49*(9), 2209–2244.
Bernard, P., & Baumont, D. (2005). Shear Mach wave characterization for kinematic fault rupture models with constant supershear rupture velocity. *Geophysical Journal International*, *162*(2), 431–447.
Bhat, H. S., Dmowska, R., King, G. C., Klinger, Y., & Rice, J. R. (2007). Off-fault damage patterns due to supershear ruptures with application to the 2001 Mw 8.1 Kokoxili (Kunlun) Tibet earthquake. *Journal of Geophysical Research*, *112*(B6).
Bouchon, M., Bouin, M. P., Karabulut, H., Toksöz, M. N., Dietrich, M., & Rosakis, A. J. (2001). How fast is rupture during an earthquake? New insights from the 1999 Turkey earthquakes. *Geophysical Research Letters*, *28*(14), 2723–2726.
Bouchon, M., & Vallée, M. (2003). Observation of long supershear rupture during the magnitude 8.1 Kunlunshan earthquake. *Science*, *301*(5634), 824–826. https://doi.org/10.1126/science.1086832
Brune, J. N., Henyey, T. L., & Roy, R. F. (1969). Heat flow, stress, and rate of slip along the San Andreas fault, California. *Journal of Geophysical Research*, *74*(15), 3821–3827.
Buades, A., Coll, B., & Morel, J. M. (2006). The staircasing effect in neighborhood filters and its solution. *IEEE Transactions on Image Processing*, *15*(6), 1499–1505. https://doi.org/10.1109/tip.2006.871137
Buades, A., Coll, B., & Morel, J. M. (2008). Nonlocal image and movie denoising. *International Journal of Computer Vision*, *76*(2), 123–139. https://doi.org/10.1007/s11263-007-0052-1
Burridge, R. (1973). Admissible speeds for plane-strain self-similar shear cracks with friction but lacking cohesion. *Geophysical Journal International*, *35*(4), 439–455.
Caniven, Y., Dominguez, S., Soliva, R., Cattin, R., Peyret, M., Marchandon, M., et al. (2015). A new multilayered visco-elasto-plastic experimental model to study strike-slip fault seismic cycle. *Tectonics*, *34*(2), 232–264. https://doi.org/10.1002/2014tc003701
Das, S. (2007). The need to study speed. *Science*, *317*(5840), 905–906. https://doi.org/10.1126/science.1142143
Dunham, E. M., & Archuleta, R. J. (2005). Near-source ground motion from steady state dynamic rupture pulses. *Geophysical Research Letters*, *32*(3).
Dunham, E. M., & Bhat, H. S. (2008). Attenuation of radiated ground motion and stresses from three-dimensional supershear ruptures. *Journal of Geophysical Research*, *113*(B8).
Ellsworth, W., Celebi, M., Evans, J., Jensen, E., Kayen, R., Metz, M., et al. (2004). Near-field ground motion of the 2002 Denali Fault, Alaska, earthquake recorded at Pump Station 10. *Earthquake Spectra*, *20*(3), 597–615.
Freund, L. B. (1998). *Dynamic fracture mechanics*. Cambridge: Cambridge University Press.
Gabuchian, V., Rosakis, A. J., Bhat, H. S., Madariaga, R., & Kanamori, H. (2017). Experimental evidence that thrust earthquake ruptures might open faults. *Nature*, *545*(7654), 336–339. https://doi.org/10.1038/nature22045
Goebel, T., Becker, T., Schorlemmer, D., Stanchits, S., Sammis, C., Rybacki, E., & Dresen, G. (2012). Identifying fault heterogeneity through mapping spatial anomalies in acoustic emission statistics. *Journal of Geophysical Research*, *117*(B3).
Gori, M., Rubino, V., Rosakis, A., & Lapusta, N. (2018). Pressure shock fronts formed by ultra-fast shear cracks in viscoelastic materials. *Nature Communications*, *9*(1), 4754. https://doi.org/10.1038/s41467-018-07139-4
Heaton, T. H. (1990). Evidence for and implications of self-healing pulses of slip in earthquake rupture. *Physics of the Earth and Planetary Interiors*, *64*(1), 1–20.
Jiang, J., & Lapusta, N. (2016). Deeper penetration of large earthquakes on seismically quiescent faults. *Science*, *352*(6291), 1293–1297. https://doi.org/10.1126/science.aaf1496
Jones, I., & Iadicola, M. (2018). A good practices guide for digital image correlation, International Digital Image Correlation Society.

Kanamori, H., & Rivera, L. (2006). in *Earthquakes: Radiated energy and the physics of faulting, edited*, pp. 3-13, American Geophysical Union, Washington. https://doi.org/10.1029/170gm03.
Latour, S., Gallot, T., Catheline, S., Voisin, C., Renard, F., Larose, E., & Campillo, M. (2011). Ultrafast ultrasonic imaging of dynamic sliding friction in soft solids: The slow slip and the super-shear regimes. *EPL (Europhysics Letters)*, *96*(5), 59003.
Lei, X., & Ma, S. (2014). Laboratory acoustic emission study for earthquake generation process. *Earthquake Science*, *27*(6), 627–646.
Liu, Y., & Lapusta, N. (2008). Transition of mode II cracks from sub-Rayleigh to intersonic speeds in the presence of favorable heterogeneity. *Journal of the Mechanics and Physics of Solids*, *56*(1), 25–50. https://doi.org/10.1016/j.jmps.2007.06.005
Lu, X., Lapusta, N., & Rosakis, A. J. (2007). Pulse-like and crack-like ruptures in experiments mimicking crustal earthquakes. *Proceedings of the National Academy of Sciences of the United States of America*, *104*(48), 18931–18936. https://doi.org/10.1073/pnas.0704268104
Lu, X., Rosakis, A. J., & Lapusta, N. (2010). Rupture modes in laboratory earthquakes: Effect of fault prestress and nucleation conditions. *Journal of Geophysical Research*, *115*(B12). https://doi.org/10.1029/2009jb006833
McLaskey, G. C., & Lockner, D. A. (2016). Calibrated acoustic emission system records M −3.5 to M −8 events generated on a saw-cut granite sample. *Rock Mechanics and Rock Engineering*, *49*(11), 4527–4536.
Mello, M., Bhat, H. S., & Rosakis, A. J. (2016). Spatiotemporal properties of Sub-Rayleigh and supershear rupture velocity fields: Theory and experiments. *Journal of the Mechanics and Physics of Solids*, *93*, 153–181.
Mello, M., Bhat, H. S., Rosakis, A. J., & Kanamori, H. (2010). Identifying the unique ground motion signatures of supershear earthquakes: Theory and experiments. *Tectonophysics*, *493*(3-4), 297–326. https://doi.org/10.1016/j.tecto.2010.07.003
Mello, M., Bhat, H. S., Rosakis, A. J., & Kanamori, H. (2014). Reproducing the supershear portion of the 2002 Denali earthquake rupture in laboratory. *Earth and Planetary Science Letters*, *387*, 89–96. https://doi.org/10.1016/j.epsl.2013.11.030
Needleman, A. (1999). An analysis of intersonic crack growth under shear loading. *Journal of Applied Mechanics*, *66*(4), 847–857.
Ngo, D., Huang, Y., Rosakis, A., Griffith, W., & Pollard, D. (2012). Off-fault tensile cracks: A link between geological fault observations, lab experiments, and dynamic rupture models. *Journal of Geophysical Research*, *117*(B1).
Nielsen, S., Taddeucci, J., & Vinciguerra, S. (2010). Experimental observation of stick-slip instability fronts. *Geophysical Journal International*, *180*(2), 697–702.
Noda, H., Dunham, E. M., & Rice, J. R. (2009). Earthquake ruptures with thermal weakening and the operation of major faults at low overall stress levels. *Journal of Geophysical Research*, *114*(B7). https://doi.org/10.1029/2008jb006143
Noda, H., & Lapusta, N. (2013). Stable creeping fault segments can become destructive as a result of dynamic weakening. *Nature*, *493*(7433), 518–521. https://doi.org/10.1038/nature11703
Olsen, K., Madariaga, R., & Archuleta, R. J. (1997). Three-dimensional dynamic simulation of the 1992 Landers earthquake. *Science*, *278*(5339), 834–838.
Passelègue, F. X., Schubnel, A., Nielsen, S., Bhat, H. S., Deldicque, D., & Madariaga, R. (2016). Dynamic rupture processes inferred from laboratory microearthquakes. *Journal of Geophysical Research: Solid Earth*, *121*(6), 4343–4365.
Passelègue, F. X., Schubnel, A., Nielsen, S., Bhat, H. S., & Madariaga, R. (2013). From sub-Rayleigh to supershear ruptures during stick-slip experiments on crustal rocks. *Science*, *340*(6137), 1208–1211. https://doi.org/10.1126/science.1235637
Rosakis, A., Samudrala, O., & Coker, D. (1999). Cracks faster than the shear wave speed. *Science*, *284*(5418), 1337–1340. https://doi.org/10.1126/science.284.5418.1337
Rosakis, A. J. (2002). Intersonic shear cracks and fault ruptures. *Advances in Physics*, *51*(4), 1189–1257.
Rosakis, A. J., Xia, K., Lykotrafitis, G., & Kanamori, H. (2007). Dynamic shear rupture in frictional interfaces-speeds,directionality, and modes, in *Treatise on Geophysics, edited*, pp. 153-192, New York: Elsevier.
Rosenau, M., Corbi, F., & Dominguez, S. (2017). Analogue earthquakes and seismic cycles: Experimental modelling across timescales.
Rubino, V., Lapusta, N., Rosakis, A. J., Leprince, S., & Avouac, J. P. (2015). Static laboratory earthquake measurements with the digital image correlation method. *Experimental Mechanics*, *55*(1), 77–94. https://doi.org/10.1007/s11340-014-9893-z
Rubino, V., Rosakis, A., & Lapusta, N. (2017). Understanding dynamic friction through spontaneously evolving laboratory earthquakes. *Nature Communications*, *8*, 15991.
Rubino, V., Rosakis, A., & Lapusta, N. (2019). Full-field ultrahigh-speed quantification of dynamic shear ruptures using digital image correlation. *Experimental Mechanics*, *1-32*.
Rubinstein, S. M., Cohen, G., & Fineberg, J. (2004). Detachment fronts and the onset of dynamic friction. *Nature*, *430*(7003), 1005–1009. https://doi.org/10.1038/nature02830
Schubnel, A., Nielsen, S., Taddeucci, J., Vinciguerra, S., & Rao, S. (2011). Photo-acoustic study of subshear and supershear ruptures in the laboratory. *Earth and Planetary Science Letters*, *308*(3-4), 424–432.
Selvadurai, P. A., & Glaser, S. D. (2015). Laboratory-developed contact models controlling instability on frictional faults. *Journal of Geophysical Research: Solid Earth*, *120*(6), 4208–4236.
Shi, Z., Ben-Zion, Y., & Needleman, A. (2008). Properties of dynamic rupture and energy partition in a solid with a frictional interface. *Journal of the Mechanics and Physics of Solids*, *56*(1), 5–24.
Singh, R. P., & Parameswaran, V. (2003). An experimental investigation of dynamic crack propagation in a brittle material reinforced with a ductile layer. *Optics and Lasers in Engineering*, *40*(4), 289–306.
Socquet, A., Hollingsworth, J., Pathier, E., & Bouchon, M. (2019). Evidence of supershear during the 2018 magnitude 7.5 Palu earthquake from space geodesy. *Nature Geoscience*, *12*(3), 192.
Song, S. G., Beroza, G. C., & Segall, P. (2008). A unified source model for the 1906 San Francisco earthquake. *Bulletin of the Seismological Society of America*, *98*(2), 823–831.
Spudich, P., & Cranswick, E. (1984). Direct observation of rupture propagation during the 1979 Imperial Valley earthquake using a short baseline accelerometer array. *Bulletin of the Seismological Society of America*, *74*(6), 2083–2114.
Sutton, M. A., Orteu, J. J., & Schreier, H. (2009). *Image correlation for shape, motion and deformation measurements: Basic concepts, theory and applications*. New York, NY: Springer.
Svetlizky, I., Bayart, E., Cohen, G., & Fineberg, J. (2017). Frictional resistance within the wake of frictional rupture fronts. *Physical Review Letters*, *118*(23), 234301. https://doi.org/10.1103/PhysRevLett.118.234301
Svetlizky, I., & Fineberg, J. (2014). Classical shear cracks drive the onset of dry frictional motion. *Nature*, *509*(7499), 205–208. https://doi.org/10.1038/nature13202
Xia, K., Rosakis, A. J., & Kanamori, H. (2004). Laboratory earthquakes: The sub-Rayleigh-to-supershear rupture transition. *Science*, *303*(5665), 1859–1861. https://doi.org/10.1126/science.1094022

Xia, K., Rosakis, A. J., Kanamori, H., & Rice, J. R. (2005). Laboratory earthquakes along inhomogeneous faults: Directionality and supershear. *Science*, *308*(5722), 681–684. https://doi.org/10.1126/science.1108193

Zheng, G., & Rice, J. R. (1998). Conditions under which velocity-weakening friction allows a self-healing versus a cracklike mode of rupture. *Bulletin of the Seismological Society of America*, *88*(6), 1466–1483.